

**Highlights 2006**

---

**Pictures on page 7** (from left to right):

Amorphous iron-based alloy with dendritic precipitations

Aluminium-based alloy

Precipitation in bulk YBaCuO

Dislocation in bulk YBaCuO

## Highlights

### Modern photoemission spectroscopy now also for high temperature superconductor $\text{YBa}_2\text{Cu}_3\text{O}_{7-\delta}$

V. Zabolotnyy, S. Borisenko, A. Kordyuk, J. Geck, D. Inosov, A. Koitzsch, J. Fink, M. Knupfer, B. Büchner, S.-L. Drechsler

We show that the photoelectron spectrum of the high temperature superconductor  $\text{YBa}_2\text{Cu}_3\text{O}_{7-\delta}$  generally includes two components: one corresponding to a highly overdoped near-surface region and the other retaining the superconducting properties. Their coexistence in angle resolved photoemission spectra was one of the reasons that caused much confusion in earlier photoemission studies of this compound. We show that choosing an appropriate excitation energy and polarization one can not only clearly identify the low energy features in the electronic structure but also suppress the intensity of the overdoped component and reveal the true superconducting one, which exhibits all the necessary attributes of superconductivity, like the gap in the density of states or unusual renormalization of the band dispersion.

Photoemission, in particular its angle resolved mode (ARPES), proved to be an indispensable tool in modern studies of high temperature superconductivity, providing detailed insight into the electronic structure and relevant many-body interactions in the systems. The method relies on the information delivered by the photoelectrons, which is contained in their energy and momentum distributions. Such type of a data carrier, however, imposes certain limitations on the technique, as the typical escape depth of several Ångströms for the emitted photoelectrons is comparable to a size of a unit cell for most of the high temperature superconductors, rendering the technique suitable only for atomically clean surfaces. Consequently, the usual way of sample preparation, which is cleaving of the crystal in ultra-high vacuum, predefines also the range of high temperature superconductors that can be successfully studied with the technique. Historically  $\text{Bi}_2\text{Sr}_2\text{CaCu}_2\text{O}_{8+\delta}$  (Bi-2212) turned to be the superconductor investigated in most details. It is this compound where the d-wave symmetry of the superconducting gap was ascertained [1] and unusual band dispersion effects were detected [2, 3]. However, when searching for features common for high temperature superconductivity in general and sieving out the irrelevant ones a thorough study of all available cuprate families is essential, and especially of those, for which the experimental data seem to disrupt the preformed general picture.

$\text{YBa}_2\text{Cu}_3\text{O}_{7-\delta}$  (YBCO-123) like all copper-oxide based high temperature superconductors is a layered material and contains two  $\text{CuO}_2$  planes per unit cell (Fig. 1). It is the first superconductor to cross the boiling point of liquid nitrogen soon after the initial discovery of high temperature superconductivity [4] and, probably, one of the most widely investigated ones. Despite this, the early photoemission studies did not turn out to be as successful as those for Bi-2212. According to LDA calculations, the bilayer-split plane derived bands and the quasi-one-dimensional band arising due to Cu-O chains are expected to be the most prominent features in the low energy electronic structure of YBCO-123. Although in some of the earliest ARPES studies [5-7] an evidence for the bilayer splitting, as well as for the chain band was reported, no clear indication for the bilayer splitting can be found in one of the most recent investigations performed with significantly improved momentum and energy resolution [8]. Contradicting attribution of the same spectral features to different bands [6-8] along with a presence of a strongly dispersing surface state and difficulties with clear observation of a superconducting gap [9] moved us still further away from complete understanding of the photoemission data for this compound. Recent observation of the resonance in the inelastic neutron scattering [10, 11] along with the above mentioned indications in early ARPES studies, renders YBCO-123 a propitious target for additional detailed ARPES investigation.

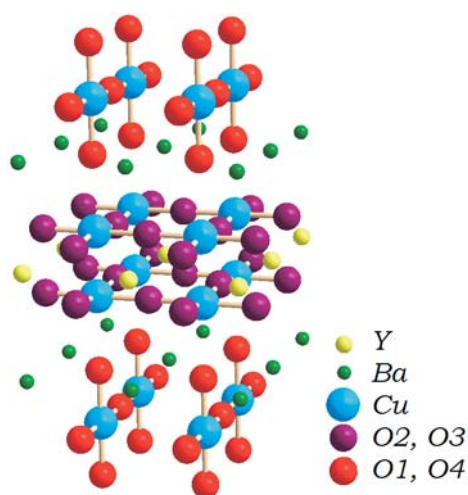
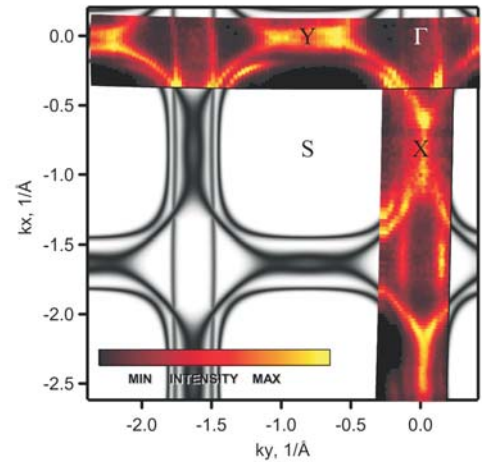
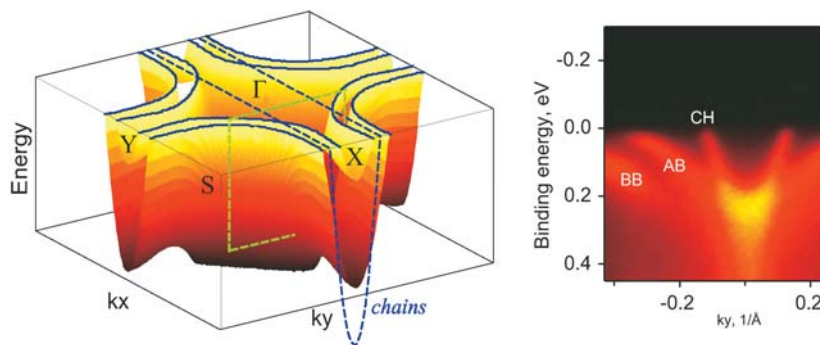


Fig. 1: Crystal structure of  $\text{YBa}_2\text{Cu}_3\text{O}_7$

Addressing the problem with improved sample quality and experimental conditions it was possible to unambiguously identify the spectral features in the YBCO-123 band structure. Similar to the other high temperature superconductors, YBCO-123 has a layered crystal structure, which results in a practically cylindrical Fermi surface, with its axis aligned along the  $k_z$  direction. For this reason, when speaking about the FS, its cut at  $k_z = \text{const}$  is normally meant. In Fig. 2 we show an experimentally obtained cut of the FS superimposed on a fitting model based on a tight binding formula for the band dispersions. Owing to an appropriate choice of the excitation energy, all the features are well pronounced and sharp, so that the two bilayer-split bands can be unambiguously identified. It is also easy to recognize that the two weaker features, parallel to  $k_x$  axis, correspond to a quasi-one-dimensional chain band. Following the predictions of the LDA calculations [12] the dispersion of all three bands can easily be traced down to energies of about 200 meV, as can be seen from Fig. 3. Though the measurements were performed at temperatures much below  $T_C$ , neither analysis of the leading edge gap positions nor the experimental band dispersion supported the existence of a superconducting gap larger than 10 meV, which is in contrast with  $T_C$  of about 90 K and nearly optimal doping of the sample. Explanation to this apparent controversy comes from the estimate of the doping level based on the FS area, which gives  $x \approx 0.30$  instead of expected  $x \approx 0.15$ . Similar overdoping of the near-surface region probed in photoemission experiment was observed in our numerous subsequent measurements for the samples with the same stoichiometry, proving this to



**Fig. 2:** Fermi surface map of  $\text{YBa}_2\text{Cu}_3\text{O}_{6.85}$ . The yellow-hot image represents the experimentally measured intensity. The two round barrels centered at S point correspond to the  $\text{CuO}_2$  plane derived bands, while the features running along  $k_x$  direction are due to the chain band.



**Fig. 3:** Schematics of the low-energy bands and the experimental spectrum of  $\text{YBa}_2\text{Cu}_3\text{O}_{7-\delta}$  clearly showing the presence of bilayer split bonding (BB), antibonding (AB) and chain (CH) bands. Green rectangle denotes the cut position in  $k$ -energy space of the reduced Brillouin zone.

be a robust effect. Therefore the overdoping effect provides a natural explanation to the problems experienced with gap observation in ARPES and STM experiments and also dispels an apparent contradiction between the high  $T_C$  for the sample and the doping level of the near-surface crystal region, most likely, modified after cleavage. The ARPES technique can also provide information concerning the thickness of the overdoped region. Analyzing the spectra more thoroughly it was found that a single EDC measured in the vicinity of the X/Y point, in addition to the two peaks from overdoped bilayer split bands, always contains an extra peak (not shown here) at energies about 40–50 meV that practically disappears above  $T_C$ , similar to the one observed in [8]. By tuning the polarization and the excitation energy it is possible to partly suppress the photoemission from the overdoped component, so that the whole spectrum attains familiar superconducting features, like those normally observed in the Bi-2212 systems [13, 14]. In particular, in Fig. 4 (a) one can see the widely discussed kinks in the band dispersion at the energy of

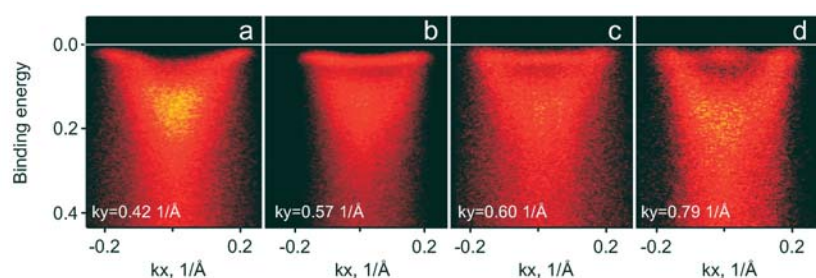


**Fig. 4:** Renormalization effects and opening of the superconducting gap in  $\text{YBa}_2\text{Cu}_3\text{O}_{6.6}$ ,  $T_C = 61$  K,  $h\nu = 50$  eV

about 50 meV. When moving closer to the Y point (panel b), similar to Bi-2212, the renormalization becomes so strong that the spectral weight gets concentrated in one practically flat and non-dispersing feature. However, in the very vicinity of the Y point the overdoped component takes over again. In panel (d) one can notice the appearance of the antibonding band of the overdoped component as well as the increase of the spectral weight at the Fermi level, which becomes especially pronounced when comparing to image (b). The fact that it is possible to detect the superconducting component in ARPES experiments tells us that the thickness of the overdoped layer is of the order of photoelectron escape depth, i.e. 5–10 Å and is comparable to one lattice spacing along the c-axis.

To conclude, we have shown that the low energy electronic structure of YBCO-123 is generally consistent with LDA calculations and that the “non-superconducting” character of ARPES spectra may result from strong overdoping of the cleaved surface. Suppressing the overdoped component in the spectra it is possible to make direct observation of a superconducting gap and the band renormalization effects similar to those observed in Bi-2212, which proves their universal character for all high temperature superconductors.

The authors would like to acknowledge Bernhardt Keimer and Vladimir Hinkov for providing the samples. We also want to thank Luc Patthey and Rolf Follath for the support during the beam times.

#### References

- [1] Ding et al., Phys Rev. B 54 (1996) 9678
- [2] P. D. Johnson et al., Phys. Rev. Lett. 87 (2001) 177007
- [3] T. Valla et al., Science 285 (1999) 2110
- [4] J. G. Bendorz, K. A. Müller, Z. Phys. B 64 (1986) 189
- [5] G. Mante et al. Phys. Rev. B 44 (1991) 9500
- [6] M. C. Schabel et al., Phys. Rev. B 57 (1998) 6090
- [7] M. C. Schabel et al., Phys. Rev. B 57 (1998) 6107
- [8] D. H. Lu et al. Phys. Rev. Lett. 86 (2001) 4370
- [9] J. G. Tobin et al., Phys. Rev. B 45 (1992) 5563
- [10] H. F. Fong et al., Phys. Rev. Lett. 82 (1999) 1939
- [11] P. Bourges et al., Science 288 (2000) 1243
- [12] O. K. Andersen et al., J. Phys. Chem. Solids 56 (1995) 1573
- [13] T. Kim et al., Phys. Rev. Lett. 90 (2003) 167002
- [14] A. Kaminski et al., Phys. Rev. Lett. 86 (2001) 1070

**Cooperation** MPI für Festkörperforschung, Stuttgart; Swiss Light Source, Paul Scherrer Inst., Villigen, Switzerland; BESSY m.b.H.

**Funded by** DFG

## New progress in flux pinning in bulk YBCO

G. Fuchs, G. Krabbes, L. Shlyk, B. Rellinghaus, C. Mickel, K. Nenkov

So far, nano-sized defects generated by irradiation techniques are the most powerful approach to very high pinning capability. In the present study, chemical attempts have been alternatively investigated to introduce into bulk  $\text{YBa}_2\text{Cu}_3\text{O}_{7-\delta}$  (YBCO) the following different types of nano-sized pinning defects using a melt-texturing process: (a) nano-scale lattice defects, (b) nano-sized particles or needles of a secondary phase, and (c) extended structures with correlated nano-sized defects showing Bose-glass behaviour. The latter ones were formed in melt-processed YBCO with Ru additions. A characteristic kink in the temperature dependence of the irreversibility line observed for applied fields  $H\parallel c$  at  $B_{cr} = 2.75$  T demonstrates Bose-glass behaviour with an average separation of correlated defects of about 30 nm. The formation of arrays of nanotwins is responsible for this behaviour as was found by TEM investigations. At fields below  $B_{cr}$ , strong flux pinning at the twin boundaries was observed if the applied magnetic field was rotated against the c-axis. For tilt angles below  $40^\circ$  the vortices were found to be strongly locked onto the twins.

The generation of pinning active defects remains a key task for the development of HTSC materials with strong flux pinning in the presence of high magnetic fields which can be used for power applications. Recent investigations have proven that the generation of columnar defects by irradiation techniques is a powerful tool to increase the pinning capability. Unfortunately, application of these methods on a large scale can hardly be expected due to the enormous technological effort, but also as a consequence of the small penetration depth of particles in dense material and the residual radioactivity in the irradiated materials. We focussed on the search for alternative chemical approaches to generate pinning centres in bulk melt-textured  $\text{YBa}_2\text{Cu}_3\text{O}_7$  (YBCO).

Flux lines are extended parallel to the applied magnetic field and have in YBCO an extremely small diameter of 4.5 nm at 77 K which is given by the coherence length of the superconductor. Therefore, defects with diameters of nanometre length scale (perpendicular to the applied magnetic field) extended along the applied field are the best candidates for strong flux pinning. The generation, handling and investigation of such small pinning centres is a challenging task.

Flux pinning in bulk YBCO can be improved by the refining of existing pinning centres, as Y-211 particles or twin structures or by creating artificial pinning centres. We have shown that artificial pinning centres with diameters of about 2 nm can be generated within the  $\text{CuO}_2$  planes by Zn or Li doping which is due to site substitution of  $\text{Cu}^{2+}$  by  $\text{Zn}^{2+}$  or  $\text{Li}^+$  [1]. Unfortunately, this site substitution is accompanied by a strong reduction of the superconducting transition temperature  $T_c$  and the irreversibility field  $B_{irr}$ . Therefore, these artificial pinning centres improve the pinning properties only in low and medium applied fields as shown in Fig. 1.

Recently, we found that extended nanoparticles can be generated in melt-textured YBCO by the addition of Ir, Ru, Ta or Hf oxides. The resulting structure consists of bands with mainly Y-211 free  $\text{YBa}_2\text{Cu}_3\text{O}_{7-\delta}$  which are separated by Me-rich phases as  $\text{YBa}_3\text{Me}_2\text{O}_9$  (Me = Ir, Ru) or perovskite like phases,  $\text{BaHfO}_3$  and  $\text{Ba}(\text{Ta},\text{Y})\text{O}_3$  in the case of Hf and Ta, respectively. The formation of the bands results from the nearly complete pushing of Y-211 from the melt and its enrichment at the propagating interface until the layer consisting of second phase particles interrupts the continuous mass flow towards the growing interface. After separation of the secondary phases the growth of the 123

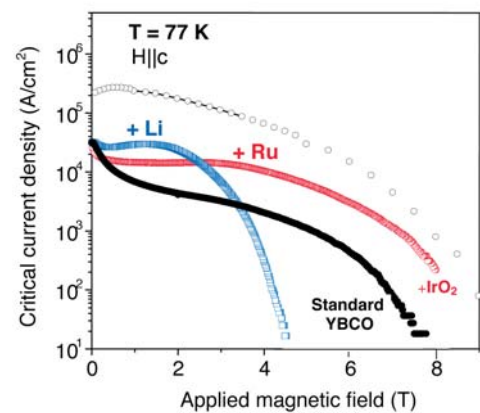
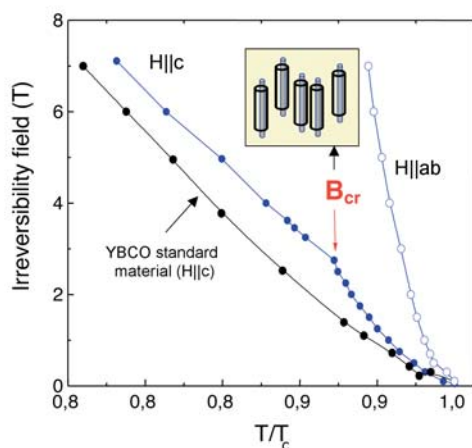


Fig. 1: Field dependence of the critical current density of bulk YBCO at 77 K for magnetic fields along the c-axis. Compared are standard YBCO (solid black symbols), Li doped YBCO (blue symbols), YBCO with additions of  $\text{RuO}_2$  and of  $\text{IrO}_2$  (red symbols) and heavy-ion irradiated YBCO with columnar defects (open black circles).



**Fig. 2:** Temperature dependence of the irreversibility field  $B_{irr}$  in bulk YBCO with (blue) and without  $\text{RuO}_2$  additions (black).  $B_{irr}$  data for two field orientations are shown. In the inset is illustrated that at the crossover field  $B_{cr}$  all correlated pins (black cylinders) are occupied by flux lines.

phase proceeds again etc. [2]. Typically, nano-sized defects have been detected within the 123 phase which is nearly free from 211 particles. For instance, by addition of 0.5 wt%  $\text{IrO}_2$ , arrays with needles of 20 – 150 nm in diameter and lengths ranging from  $\mu\text{m}$  to tenths of  $\mu\text{m}$  were obtained. These needle-shaped artificial pinning centers are inhomogeneously distributed in the sample. They improve the pinning properties in the whole field range up to the irreversibility field  $B_{irr}$  which is even slightly enhanced in comparison to that of the YBCO standard material as shown in Fig. 1.

We also succeeded in the generation of extended and correlated nanoparticles. The samples were prepared by adding of 0.25 – 0.40 wt%  $\text{RuO}_2$  to YBCO. Similar as in the case of  $\text{IrO}_2$ , the addition of  $\text{RuO}_2$  significantly alters the melt properties and the growth behavior resulting in a periodically grown structure of nearly 211-free YBCO and Ru-rich phases [3]. We found clear indications of a Bose glass phase in this material. In contrast to the usual vortex glass phase consisting of strongly deformed flux lines, a Bose glass phase consists of straight flux lines which is due to their strong interaction with correlated nano-defects. Bose glass behaviour is characterized by a kink in the temperature dependence of the irreversibility field  $B_{irr}(T)$  observed in this material for fields along the c-axis (see Fig. 2). Below the so-called crossover field  $B_{cr}$  at which this kink is observed, all flux lines are strongly pinned on correlated pins. At  $B_{cr}$ , all correlated pins are occupied by flux lines. Therefore, the additional flux lines appearing at higher fields locate between the strongly pinned flux lines. From the spacing of flux lines at  $B_{cr}$ , one estimates for the correlated defects an average separation of  $d \approx (\phi_0 / B_{cr})^{0.5} \approx 30 \text{ nm}$ . For this material, similar critical current densities were found as obtained by addition of 0.5 wt%  $\text{IrO}_2$  (see Fig. 1).

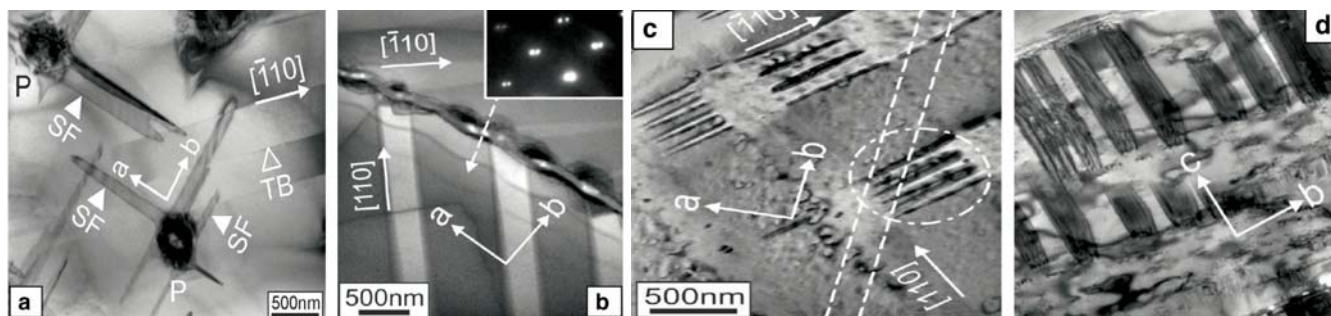


**Fig. 3:** Analysis of the microstructure of bulk YBCO with  $\text{RuO}_2$  additives. (a) TEM bright field image of stacking faults (SF) in the  $a$ - $b$  plane emerging from  $\text{YBa}_3\text{Ru}_2\text{O}_9$  precipitates (P). The planar defects are several  $\mu\text{m}$  long and may cross neighboring twin boundaries (TB). (b) Twin lamella occurring on both sides of a nanocrystalline band. A dashed arrow indicates that part of the sample where the SAD pattern (see inset) is taken from. (c) Complex twin boundary in the  $a$ - $b$  plane with arrays of accommodation nanotwins. Dashed lines and circle indicate the region represented in the  $b$ - $c$  plane view in (d) with the same magnification.

The microstructure of this bulk YBCO with Bose glass behaviour was determined by scanning and transmission electron microscopy (TEM) utilizing a *Philips XL30* and a *JEOL FX2000* microscope, respectively. Whereas the amount of Y-211 particles is drastically reduced in this material, additional precipitates of  $\text{YBa}_3\text{Ru}_2\text{O}_9$  particles, about 200 nm in size, have been found surrounded by crossed planar defects (see Fig. 3a.) which have been identified as stacking faults. These defects extending in the  $a$ - $b$  planes have only weak pinning capability. We observed another type of Ba-rich precipitates (with  $\text{Y}:\text{Ba}:\text{Cu} \approx 1:5:1$ ) which is arranged in roughly 10 nm thick bands extending over larger areas. The stress between such bands is particularly high at the interface to the YBCO matrix resulting in the formation of twins with perpendicular orientation on both sides of the band as shown in Fig. 3b. Fig. 3c displays the formation of accommodation nanotwins which were observed within these complex twin boundaries. The nanotwins are significantly smaller than the well-known primary twins. They are *periodically arranged within the crossing of two primary twins* and the average distance between subsequent nanoscale twin boundaries is roughly 60 nm. The spacing of these small nanotwins is comparable with the average separation of correlated defects estimated from the crossover field  $B_{cr}$ . Therefore, we believe that these nanotwins are responsible for the Bose glass behavior in this material. As can be seen from Fig. 3d, the accommodation twins are extended along the  $c$  direction and have a length of several  $\mu\text{m}$ .

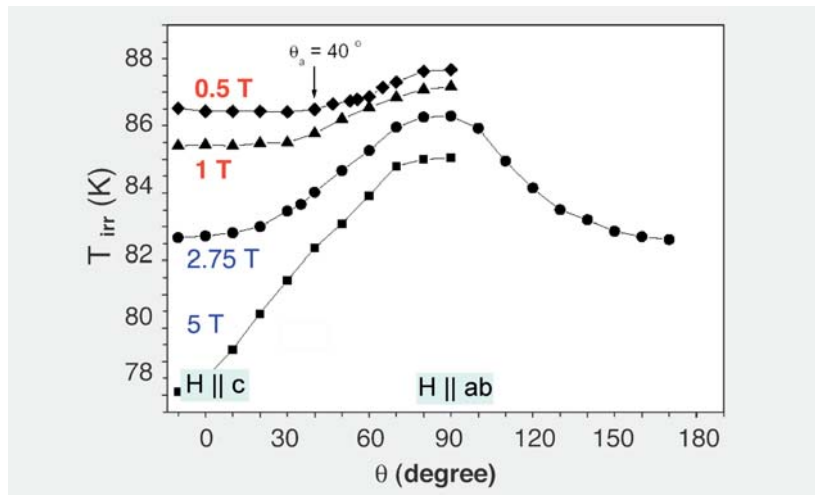


Fig. 4: Irreversibility temperature of YBCO with a periodical array of nanotwins at fixed values of the applied magnetic field as function of the angle between the applied field and the  $c$ -axis.

We studied the angle dependence of the irreversibility temperature  $T_{irr}$  at fixed magnetic fields by rotating the  $c$ -axis of the sample against the applied magnetic field (see Fig. 4). For applied fields exceeding the crossover field, a continuous variation of  $T_{irr}$  for increasing angle is observed indicating that the flux lines in the superconductor exactly follow the rotating applied field. Below the crossover field,  $T_{irr}$  remains constant in a wide angle range up to about  $40^\circ$  starting from fields along the  $c$ -axis. This means that the flux lines are strongly locked onto the twins as illustrated in Fig. 5 for one flux line.

These results demonstrate that chemical alterations of melt-textured YBCO can initialize arrays of extended and correlated pinning centers. A Bose glass state was found in bulk YBCO with arrays of nanotwins which was known so far only for columnar tracks obtained by irradiation with high-energy particles.

## References

- [1] L. Shlyk, G. Krabbes, G. Fuchs, K. Nenkov, P. Verges: Appl. Phys. Lett. 81 (2002) 5000.
- [2] L. Shlyk, B. Schüpp, G. Krabbes, K. Nenkov, G. Fuchs: Physica C 406 (2004) 107
- [3] L. Shlyk, G. Krabbes, G. Fuchs, C. Mickel, B. Rellinghaus, K. Nenkov: Appl. Phys. Lett. 88 (2006) 062509

Cooperation Atominstitut Wien, Univ. Houston, Univ. Cambridge, MAI Moskau, Oswald Elektromoren GmbH Miltenberg

Funded by BMBF, British Research Council

$T_{irr} = \text{const.}$  ( $\Theta < 40^\circ$ )  
 → flux lines are "locked" onto the twins

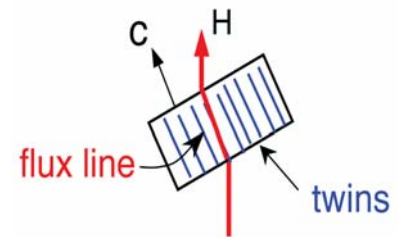


Fig. 5: Shape of a flux line in YBCO with Bose glass behavior for applied fields below the crossover field in the angle region of constant  $T_{irr}$  (see Fig. 4). The flux line is locked onto the twins parallel to the  $c$ -axis in spite of the rotation of the  $c$ -axis against the applied magnetic field.

## YBa<sub>2</sub>Cu<sub>3</sub>O<sub>7-δ</sub> films with artificial pinning centres for Coated Conductor applications

B. Holzapfel, E. Backen, S. Engel, R. Hühne, T. Thersleff, L. Schultz

To improve the critical current density of YBa<sub>2</sub>Cu<sub>3</sub>O<sub>7-δ</sub> (YBCO) films in magnetic fields, nanometre scaled pinning sites have to be introduced into the YBCO matrix. Here we present a new method to introduce highly effective pinning sites into YBCO by preparing metal/YBCO quasimultilayer structures using Pulsed Laser Deposition (PLD). With this technique, the creation of pinning-effective BaHfO<sub>3</sub> nanoparticles is demonstrated, leading to a shift of the irreversibility line of up to 4 T over a wide temperature range. Chemical Solution Deposition (CSD) techniques were also applied to create these pinning sites by a scalable film preparation approach, which is needed for coated conductor production. Interestingly, not only were high critical current densities reached over a wide field range, but, even more importantly, the absence of pinning anisotropy behaviour created defect arrangements that resulted in a complete isotropic J<sub>c</sub>-behaviour in low and medium magnetic fields at 77 K.

High Temperature Superconductor (HTSC) based wires and tapes offer a variety of interesting opportunities for electrical power applications. Power transmission cables, motors, generators and transformers can be built much smaller and more powerful using HTSC wires or tapes. To realize these applications, the necessary HTSC wires and tapes require a high critical current density (J<sub>c</sub>) and a large volume, low cost production route. The coated conductor approach (Fig. 1), where a high J<sub>c</sub> YBCO film is deposited onto a highly biaxially textured metal tape template, meets both of these materials science and economic challenges. Currently, research and development projects are running worldwide to develop this technique and transfer it to wire production level.

One very successful approach is to use metal tapes based on fcc materials as substrates, which show a high degree of biaxial texture – the so-called cube texture – after strong cold deformation and recrystallization. At the IFW Dresden, this approach was successfully developed for Ni-alloys (e.g. Ni-5at%W) [1] and also commercialized by the foundation of a spin-off company named evico GmbH [2], which, since 2004, has been producing and selling these tapes to a number of international companies and research institutions working in this field. The high texture of these metal tape templates is transferred via epitaxial film growth of oxide buffer layers to the YBCO film. Critical current densities above 1 MA/cm<sup>2</sup> at 77 K and self-field can be obtained with these coated conductors – values that are as high as for YBCO thin films on single crystalline substrates. A further improvement of the critical current density of YBCO coated conductors in magnetic fields requires enhanced intragrain pinning due to the grain-based electrical current limiting mechanism at higher fields [3]. Due to the short coherence length in high temperature superconductors, nano-sized precipitates are necessary to act as effective pinning centers in YBCO. Last year we developed a new technique to introduce nano-scaled particles into the YBCO matrix by depositing quasimultilayers (multilayer heterostructures, in which one layer is incomplete and forms nucleation

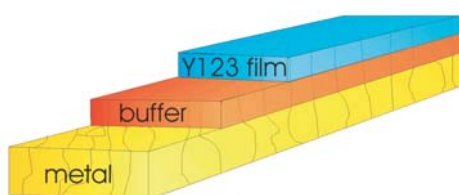
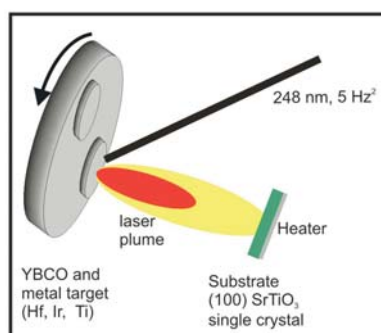
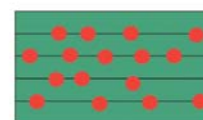


**Fig. 1:** Schematic drawing of the coated conductor approach. Onto a highly biaxial textured metal tape, buffer layers and a superconducting YBCO layer are epitaxially grown to reach high critical current densities above 1 MA/cm<sup>2</sup> at 77 K and self-field.



L x (m pulses YBCO / n pulses TM)

TM = Ir, Hf, Ti



➔ Formation of YBCO/BaTMO<sub>3</sub> quasi-multilayers

**Fig. 2:** Preparation of quasimultilayer films using PLD

islands) of YBCO and a metal (ME=Ir, Ti, Hf) by PLD as shown in Fig. 2 [4]. The deposited metal sub-monolayers react under the deposition conditions with the YBCO matrix to form nano-scaled inclusions with the perovskite structure  $BaMEO_3$ . These inclusions are epitaxially incorporated into the YBCO matrix.

Whereas doping with Ti shows no  $J_c$  improvement in higher magnetic fields and doping with Ir only shows only marginal improvement, the quasimultilayers containing  $BaHfO_3$  exhibits, for some samples, very high irreversibility fields above 10T. The temperature dependence of the irreversibility field reveals a constant strong shift of 4T compared to undoped YBCO (Fig. 3). These effects are comparable to the introduction of irradiation-based columnar defects, the strongest pinning centers for YBCO known so far. The observed behaviour is typical for the formation of a Bose glass as discussed in detail by G. Fuchs in this annual report for YBCO bulk material.

Using off-axis pulsed laser deposition, a significant improvement in reproducibility of these effects was obtained. The measurement of the full  $J_c$ -anisotropy with respect to the direction of the applied magnetic field for Hf-doped quasimultilayers reveals a strong  $J_c$  maximum at field orientations parallel to the YBCO c-axis as shown in Fig. 4. This B II c maximum of the critical current density indicates a self alignment of individual nanoparticles to rod-like arrays during the film deposition due to strain effects during nucleation.

Since this quasimultilayer approach using PLD is not applicable as a low cost deposition process, we investigated other film deposition techniques to introduce pinning effective  $BaHfO_3$  nanoparticles. We were able to demonstrate that the metal-organic deposition technique can be modified to be used as a cost-effective and highly versatile method for introducing nanosized pinning centres to YBCO [6]. The TFA-YBCO route with Hf-enriched precursor solutions was used to segregate nano-sized  $BaHfO_3$  particles during the reaction. Both the YBCO film and the  $BaHfO_3$  particles grow with a biaxial texture in a cube-on-cube relationship. Investigations into the behaviour of the critical current density in magnetic fields up to 9 T reveal a strong enhancement of  $J_c$  at high magnetic fields with increasing amounts of  $BaHfO_3$  precipitates. Pinning centres introduced by Chemical Solution Deposition (CSD) techniques display enhanced pinning properties in all magnetic fields compared to PLD techniques, where often a zero field reduction of  $J_c$  is observed in films with pinning-active nanoscale precipitates as shown in Fig. 5. Even more interesting is the  $J_c$  anisotropy of the Hf-doped CSD films as shown in Fig. 6. It is not only apparent that at low magnetic fields the critical current density for B II c is larger than the intrinsic pinning peak at B II ab but also that, at fields up to several Tesla, there is a very unusual isotropic  $J_c$ -dependence present. In contrast to the Hf-doped PLD quasimultilayers, this isotropic  $J_c$  enhancement indicates a random distribution of

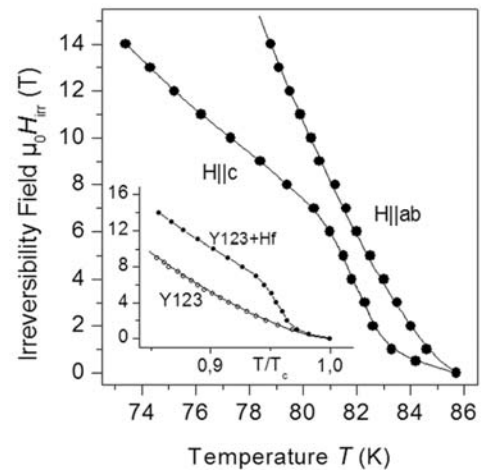


Fig. 3: Temperature dependence of the irreversibility field  $B_{ir}$  in YBCO thin films with and without nanoscaled  $BaHfO_3$  precipitates.

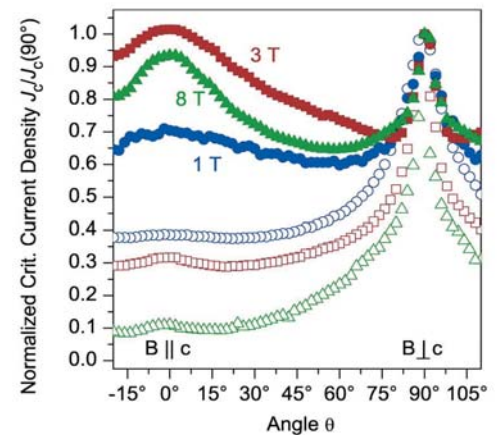


Fig. 4:  $J_c$ -Anisotropy of quasimultilayers containing  $BaHfO_3$  nanoparticles (closed symbols).

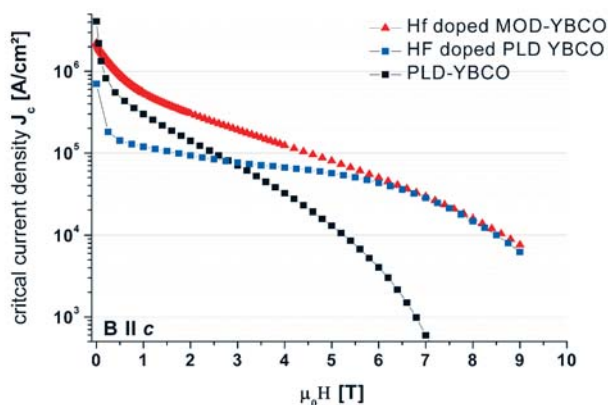


Fig. 5: Magnetic field dependence of YBCO films containing  $BaHfO_3$  nanoparticles, prepared by PLD (blue) or by CSD (red). For comparison, a standard YBCO film is shown (black).

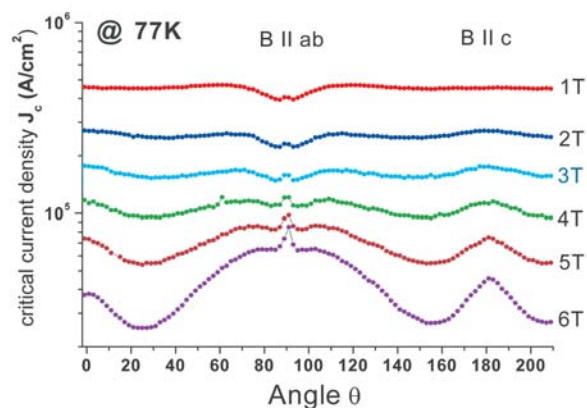


Fig. 6:  $J_c$ -Anisotropy for different magnetic fields of YBCO thin films prepared by CSD containing  $BaHfO_3$  nanoparticles.

highly effective pinning centres. Ongoing High Resolution TEM investigations will reveal the details of the pinning-active defects and their distribution both in PLD quasi-multilayers and Hf-doped CSD films.

In summary, very effective pinning centres were introduced into YBCO films by incorporating epitaxially nano-scaled BaHfO<sub>3</sub> precipitates both by pulsed laser deposition and the cost-effective and highly versatile chemical solution deposition technique. High irreversibility fields at 77 K above 9 T and an isotropic critical current density can be obtained using chemical solution deposition, which is currently one of the most favourable deposition techniques for coated conductor commercialization.

#### References

- [1] J. Eickemeyer, D. Selbmann, R. Opitz, B. de Boer, B. Holzapfel, L. Schultz and U. Miller, *Supercond. Sci. Technol.* 14, 152 (2001)
- [2] for more details see [www.evico.cc](http://www.evico.cc)
- [3] L. Fernandez, B. Holzapfel, F. Schindler, B. De Boer, A. Attenberger, J. Hänisch, and L. Schultz, *Phys. Rev. B* 67, 052503 (2003)
- [4] J. Hänisch, C. Cai, R. Hühne, L. Schultz, and B. Holzapfel, *Appl. Phys. Lett.* 86, 122508 (2005)
- [5] J. Hänisch, C. Cai, V. Stehr, R. Hühne, J. Lyubina, K. Nenkov, G. Fuchs, L. Schultz, and B. Holzapfel, *Supercond. Sci. Technol.* 19, 534 (2006)
- [6] S. Engel, T. Thersleff, R. Hühne, L. Schultz and B. Holzapfel, *Appl. Phys. Lett.*, in press

**Cooperation** ICMAB Barcelona, Atominstytut Wien, Univ. Cambridge

**Funded by** BMBF, EU

## A new type of stripe structure in $\text{Na}_x\text{CoO}_2$

K. Koepernik, J. Geck, M. v. Zimmermann, H. Berger, S.V. Borisenko, H. Eschrig,  
M. Knupfer, B. Büchner

A combined high-energy x-ray diffraction and LDA study of the sodium ordering in  $\text{Na}_{0.75}\text{CoO}_2$  has been performed. The obtained results rule out previously proposed Na-ordering models and provide strong evidence for the formation of sodium-density stripes in this material. The LDA calculations prove, that the sodium-density stripes lead to a sizeable dip in the Co-density of states at the Fermi level, pointing to band structure effects as a driving force for the stripe formation. This indicates that the sodium ordering is connected to stripe-like charge correlations within the  $\text{CoO}_2$  layers, leading to an intriguing similarity between the doped cuprates and the  $\text{Na}_x\text{CoO}_2$  compounds.

Recently the correlated electron system  $\text{Na}_x\text{CoO}_2$ , has attracted considerable attention, due to the discovery of superconductivity in water-intercalated compounds [1] as well as the interesting physics of the non-hydrated materials. For  $x > 0.5$  an anomalously large thermopower, the coexistence of localized moments and electron itinerancy as well as unusual charge and spin order phenomena have been reported.

Many body effects in correlated electron systems may result in intrinsic charge inhomogeneities. A very prominent example is the so-called stripe ordered phase in the cuprates, where the doped holes condense into charge stripes within the physically relevant  $\text{CuO}_2$ -planes [2]. Up to date, this stripe order is discussed intensively in relation to the high-temperature superconductivity and the anomalous metallic state of these materials.

In order to answer the question whether the unconventional physical properties of  $\text{Na}_x\text{CoO}_2$  with  $x \sim 0.7$  are also related to the presence of charge inhomogeneities (which are formed within the  $\text{CoO}_2$ -layers in this case) we performed a detailed characterization of structural modulations in high-quality  $\text{Na}_{0.75}\text{CoO}_2$  single crystals by means of high-energy x-ray diffraction (HXD), which has been proved to provide a highly sensitive probe for the extremely weak structural modulations related to the formation of charge inhomogeneities [3].

During a survey in reciprocal space, a number of superstructure reflections were observed around the (100) reflection in the (hk0)-plane, which are summarized in Fig. 1. The open circles represent the Bragg reflections of the basic hexagonal lattice, as indicated by the reciprocal lattice vectors  $\mathbf{b}_{1,2}$ , which correspond to the direct lattice vectors  $\mathbf{a}_{1,2}$  parallel to the Na- and  $\text{CoO}_2$ -layers (cf. Fig. 2). The solid circles represent superstructure peaks observed for all investigated temperatures, while the hatched circles represent peaks only observable below  $T_{S0} = 350$  K. A correlation length of about 300 Å for the corresponding superstructure modulation has been determined.

The two superlattice peaks, named P1 and P2 in Fig 1, show a distinct behavior in temperature dependent measurements. The most pronounced difference is the vanishing of the intensity of the peak P2 above  $T_{S0}$ , while the intensity of the peak P1 is comparatively constant in the whole measured temperature range. In addition to this, the intensity of the P2 reflection depends strongly on the cooling process, which is a strong indication that the ordering phenomenon corresponding to the occurrence of the P2 reflection is related to the sodium ions: due to the relatively slow Na ion-hopping processes a certain amount of the high temperature sodium disorder is frozen upon rapid cooling while a superstructure can form to a higher extent if the sample is cooled down slowly.

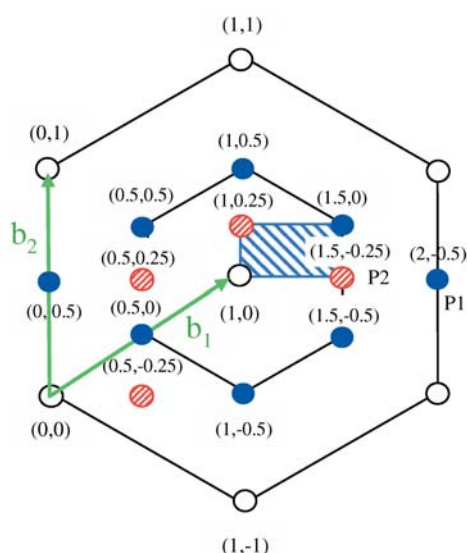


**Fig. 1:** Summary of observed superstructure peaks around (100). The hatched rectangle marks the assumed unit cell of the reciprocal lattice.

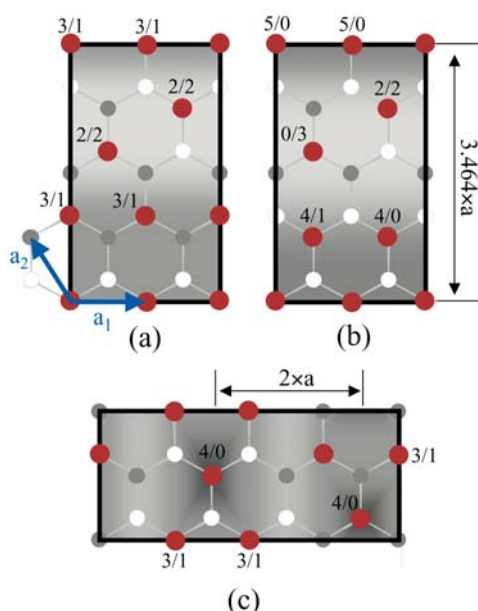


**Fig. 2:** Models for the sodium superlattice in  $\text{Na}_{0.75}\text{CoO}_2$ . Projections of superstructure unit cells on the  $(\mathbf{a}_1, \mathbf{a}_2)$ -plane are shown. Small gray and white circles indicate Na(1)- and Na(2)-sites, respectively. The occupied Na-sites are indicated by big solid (red) circles. The numbers  $m/n$  indicate the number of first/second Na-Na neighbors and the corresponding sodium-density variations are indicated by the gray shadings.

One can conclude that the low temperature superstructure is established in two steps: First, the doubling of the unit cell signaled by the P1 reflection at temperatures well above 360 K, followed by the structural modulation related to the P2 peak appearing below  $T_{S0} = 350$  K, which can clearly be attributed to sodium order.

The observed superlattice reflections in the  $(hk0)$ -plane can be described by the orthogonal basis vectors  $\mathbf{b}_1/2 - \mathbf{b}_2/4$  and  $\mathbf{b}_2/4$ , as indicated by the hatched rectangle in Fig. 1. Although the HXD data do not prove unambiguously the dimensions of the unit cell, important clear-cut conclusions regarding previously proposed models for the sodium ordering in  $\text{Na}_{0.75}\text{CoO}_2$  can be drawn: The superlattice reflections corresponding to the unit cell, which was deduced from electron diffraction (ED) data [4] and which was used later for ab initio calculations [5] [6] are not observed. The superstructure related to the vacancy ordering that has been found in Monte Carlo simulations [7] does also not match our HXD results.

In order to further clarify the situation, we performed an LDA study of the sodium order. Figs. 2 (a),(b) are based on the supercell, which corresponds to reciprocal lattice vectors  $\mathbf{b}_1/2 - \mathbf{b}_2/4$  and  $\mathbf{b}_2/4$ , while Fig. 2 (c) corresponds to the lowest energy state reported by Zhang et al. based on the unit cell deduced from ED data [4] [5]. The calculations yield the lowest total energy for the structure given in Fig. 2 (a), while the two structures shown in Fig. 2 (b) and (c) correspond to higher total energies.

The differences between the structures (a), (b) and (c) can essentially be understood by Coulomb energy arguments: (a) and (c) comprise a charge density wave of comparable amplitude, but with wave vector  $2\mathbf{a}_1 + 4\mathbf{a}_2$  in the case (a), while (c) has the shorter wave vector  $2\mathbf{a}_1$ . The structure (b) has also a charge density wave with wave vector  $2\mathbf{a}_1 + 4\mathbf{a}_2$ , however with a considerably larger amplitude.

Since the model by Zhang Fig. 2 (c) neither corresponds to the superstructure reflections observed by HXD nor has the lowest total energy, we can exclude this ordering pattern as a ground state for  $\text{Na}_{0.75}\text{CoO}_2$ . The same excluding arguments hold for the structure determined by Meng et al. [6].

The disagreement between the ED and the HXD data mentioned above could be due to the different sample volumes probed by the two techniques. The penetration depth in our HXD study is of the order of 1 mm and therefore guarantees the detection of bulk properties, while it is of the order of 100 nm in the case of ED. Furthermore, the electron beam used for the ED experiment itself might influence the sodium ordering [4].

The transition temperature  $T_{S0}$  found in the present HXD study is in good agreement with the sodium rearrangement that was observed by neutron powder diffraction [8], further supporting the conclusion that the superlattice modulation below  $T_{S0}$  is not primarily related to charge order within the  $\text{CoO}_2$ -layers but to sodium order.

The obtained lowest energy state (a) exhibits sodium density stripes (SDS) within the Na-planes, as indicated by the gray shading in Fig. 2. The LDA calculations prove, that this ordering produces a sizeable dip in the Co-density of states at the Fermi level, pointing to band structure effects as a driving force for the stripe formation. This indicates that the SDS are related to intrinsic stripe-like charge correlations within the  $\text{CoO}_2$ -planes, which is also supported by an NMR/NQR study, where different Co-sites were observed for  $\text{Na}_x\text{CoO}_2$  with  $x \sim 0.7$  [9].

Taking into account that the hydrated superconducting samples are of the composition  $\text{Na}_{0.337}(\text{H}_3\text{O})_2\text{CoO}_2 \cdot y\text{H}_2\text{O}$  with a doping level corresponding to  $\text{Na}_x\text{CoO}_2$  with  $x \sim 0.7$  [10],

an intriguing analogy to the high-temperature superconducting cuprates appears: The electric field that is caused by the SDS might induce a pinning potential for charge stripes within the adjacent  $\text{CoO}_2$  layers, similar to the cooperative octahedral tilts in the so-called LTT-phase of the doped cuprates. One may speculate whether the reduction of this pinning potential upon hydration is related to the concomitant appearance of superconductivity. However, this scenario has certainly to be verified by further experiments.

In conclusion, our study can clearly rule out previous proposed sodium order models for  $\text{Na}_{0.75}\text{CoO}_2$ . Furthermore, the experimental and theoretical results provide firm evidence for the development of SDS below  $T_{S0}$ , which is related to charge-stripe correlations within the two-dimensional triangular  $\text{CoO}_2$ -layers.

### References

- [1] K. Takada et al.: Nature 422 (2003) 53
- [2] J. Orenstein and A. Millis: Science 288 (2000) 468
- [3] J. Geck: Phys. Rev. Lett. 97(10) (2006) 106403
- [4] H. W. Zandbergen et al.: Phys. Rev. B 70 (2004) 024101
- [5] P. Zhang et al.: Phys. Rev. B 71 (2005) 153102
- [6] Y. Meng et al.: Phys. Rev. B 72 (2005) 172103
- [7] M. Roger et al.: cond-mat/0507040 (2005)
- [8] Q. Huang et al.: Phys. Rev. B 70 (2004) 134115
- [9] I. R. Mukhamedshin et al.: Phys. Rev. Lett. 94 (2005) 247602
- [10] C. J. Milne et. al.: Phys. Rev. Lett. 93 (2004) 247007

**Cooperation** HASYLAB at DESY Hamburg, Institut de physique de la matière complex (IPMC), EPF Lausanne, Switzerland

**Funded/supported by** Swiss NCCR research pool MaNEP of the Swiss NSF, DFG (SFB 463, FOR 538)

## Theoretical prediction of a skyrmion ground state in chiral magnets

U. K. Rößler, A. N. Bogdanov

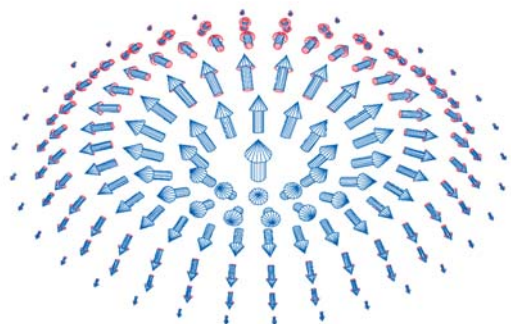


Fig. 1: Cross-section through a magnetic Baby-Skyrmion string.

In certain non-linear field models particle-like states, so-called Skyrmions, can be stabilized. We have found that a basic continuum theory for magnetic states in non-centrosymmetric magnets may allow unusual phases, which are formed by the condensation of such Skyrmions. These skyrmionic ground states have the appearance of modulated spin-textures and they are chiral. This result is unexpected as one had previously believed that such multiply twisted magnetization structures generally are unstable. The theoretical result may explain some recent experimental observation in the chiral helixmagnet MnSi. However, skyrmionic ground states may exist in many other magnetic systems, including thin films made of conventional magnetic materials. Beyond magnetism, our theory may have wider implications because the mechanism stabilizing skyrmionic states relies only on a tendency to form twisted states in chiral condensed matter systems.

The occurrence of countable particles in continua is a deep problem in fundamental or less fundamental physical theories aiming at a mathematical description of a world composed of particles that should exist in continuous space and time. Therefore, theoreticians were always intrigued by solutions of field theories with a particle-like structure. Interestingly, many theoretical models in physics cannot form such states. T.H.R. Skyrme showed, in a work on nuclear matter, how the desired stable localized solutions with the appearance of a particle and a physical size can be derived within a field theory model for elementary particles. Therefore, such stable states are now named „Skyrmions“.

In condensed matter systems, Skyrmions and extended Skyrmionic textures exist, e.g., under non-equilibrium conditions in turbulent fluids, induced by external fields in Quantum Hall magnets, or stabilized by topological defects in the blue phases of chiral liquid crystals.

We have derived theoretical results on novel Skyrmionic magnetization structures in magnets with broken inversion symmetry. In these chiral systems, a particular exchange, so-called Dzyaloshinskii-Moriya interactions, stabilizes Skyrmions [1]. The chiral Dzyaloshinskii-Moriya couplings are weak compared to the direct magnetic exchange, but they lead to a twisting of magnetic states. Up to now, it was believed that only a one dimensional modulation of the magnetization can be formed in such chiral crystals. The metallic compound MnSi with a cubic non-centrosymmetric B20-structure is the best-known example of such a chiral magnet. The magnetic order in MnSi is essentially ferromagnetic, but the weak Dzyaloshinskii-Moriya interactions lead to a slightly twisted magnetization distribution with the shape of a flat helix and a rather long period of a few nanometers.

Our demonstration that more complex states with multiple twist can exist in such chiral magnets was based on the finding that string-like vortex-Skyrmions (or Baby-Skyrmions) are stable states. These Baby-Skyrmions are localized in two dimensions only. We could show that these states form stable condensates in a phase diagram of a simple model for ferromagnetic metals. This was sufficient to prove the appearance of a skyrmionic phase between the paramagnetic and the helixmagnetic state in chiral magnets. Our continuum model requires as a crucial ingredient a generalization of the commonly used exchange energy by a softened stiffness for the modulus of the local magnetization. This condition is apparently met in (weakly) magnetic metals. The mechanism leading to a formation of multiply twisted particle-like states or vortices is illustrated in Fig. 1. The magnetization of these strictly localized solutions becomes zero at the border of these objects with cylindrical symmetry. These Skyrmionic objects form

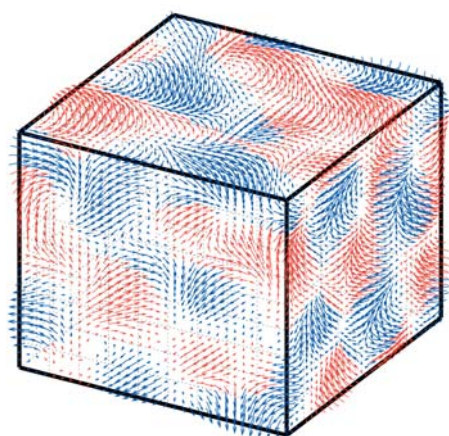


Fig. 2: Three dimensional magnetization texture in a chiral cubic magnet from a numerical simulation.

dense textures and in such a condensate the Skyrmions may have attractive and repulsive interactions, which lead to certain elastic deformations at their rim. However, the core region of these Skyrmions remains stable. Hence, these condensates resemble a liquid or solid composed of molecular objects, as in Fig.2. However, here the formation of a condensate from countable units takes place in a continuum!

Our theory gives an explanation of the „partial magnetic order“, recently found in experiments on MnSi under high pressure. We suggest that a Skyrmionic texture with an amorphous or liquid appearance is a ground-state in this weakly ferromagnetic metal owing to its non-centrosymmetric crystal structure. Moreover, we predict that magnetic Skyrmion lattices exist quite generally in magnetic films owing to the broken inversion symmetry at surfaces. For these systems, the two-dimensional model composed of Baby-Skyrmions is relevant, and we predict that close to the magnetic ordering-temperature one should find Skyrmions in thin films at least for weakly magnetic metals and in the case of low magnetic anisotropy. Higher anisotropies would block the propensity of the magnetization to twist under influence of the chiral exchange.

Ground states from multiply twisted structures, as in Fig. 1, are generally expected for certain classes of condensed matter systems with broken inversion symmetry. They are not restricted to magnetic systems. The basic multiply twisted Skyrmionic objects have been known for chiral nematic liquid crystals for a long time already. Double-twist cylinders with properties of Baby-Skyrmion strings in these complex liquids are responsible for the formation of the so-called blue phases. They can be described as dense interwoven textures of double-twist cylinders and certain stabilizing topological defects. However, two mechanisms must conspire to produce such textures in general cases as in the non-centrosymmetric magnets: (i) Chiral couplings must be present, which take in phenomenological continuum theories antisymmetric forms, that are known as Lifshitz invariants. (ii) The modulus of the order parameter, here the magnetization, has to be soft enough to be driven to zero locally. The latter mechanism stands in for the topological defects that would be required for the formation of multiply twisted extended textures in the case of a fixed modulus of the order-parameter. Hence, we expect that multiply twisted mesophases with similar textures may exist in condensed matter as varied as some ferroelectrics, multiferroic materials, metallic glasses. Skyrmionic states could also be associated with certain structural phase transitions breaking inversion symmetry.

## References

- [1] U.K. Rößler, A.N. Bogdanov, C. Pfleiderer, *Nature* **442** (2006) 797

**Cooperation** C.Pfleiderer, TU München, Donetsk Institute for Physics and Technology, Donetsk Ukraine

## Micromagnetic coupled pendulums in magnetic thin film arrays

J. McCord, I. Mönch, R. Schäfer, L. Schultz

By adjusting the magnetic domain states in square ferromagnetic elements, a coupled micromagnetic system with GHz oscillation frequency similar to that of coupled pendulums can be generated. The occurrence of coupling is associated with spire domains at the element's edges. Dynamic mode-to-mode energy transfer results in a precessional decay time exceeding the natural ferromagnetic relaxation time of the material. This reduction in effective magnetic damping is in contradiction to the consensus that magnetic domain formation leads to a decrease in precessional relaxation time. The observed behavior possesses great technological impact for the understanding of the high-frequency behavior of devices in spintronics, in particular the performance of yokes in magnetic recording write heads.

In classical mechanics, a simple harmonic oscillator experiences a sinusoidal oscillation with a characteristic frequency, once it is displaced from its equilibrium position. Adding a second oscillator to the system, the oscillations can be considered a superposition of two natural oscillations. This has consequences for the dynamics of the system. For instance, during the oscillation of two undamped coupled pendulums, the oscillation energy is transferred from one pendulum to the other. In the idealistic case of two equal pendulums, for which the initial oscillation is started with one pendulum while the other is at rest, the energy is transferred completely from one pendulum to the other and finally back again. In real systems, however, friction or damping occurs, resulting in a damped oscillation with a typical exponential decay in amplitude over time. Non-equal pendulums change the response of the coupled system even more. Besides mechanics, nature and physics provide numerous additional examples of coupled oscillations. Best known are resonant or RLC circuits in electrodynamics, consisting of a resistor, an inductor, and a capacitor.

Comparable oscillations as for a damped oscillator are observed in magnetization dynamics. Once the magnetization is moved from its equilibrium position, a gyroscopic precession of magnetization with a characteristic resonance frequency  $f_{\text{res}}$  takes place. A damping torque is responsible for the reorientation of magnetization into its equilibrium position. Immediately the similarity to the mechanical motion problem becomes obvious. In research, mode-mode interaction of small micromagnetic systems has gained particular attention. Past experiments focused on small ferromagnetic Permalloy® thin film elements with the most simple flux closure domain pattern [1]. The domain formation in larger elements (some 10 micrometer lateral extension) is more complicated and the exhibited domain structures strongly depend on the magnetic anisotropy of the material and on magnetic field history. For such extended structures we could recently show that an increase in domain density directly translates into a positive precessional frequency shift due to magnetostatic interactions introduced by the domain walls [2]. Based on this work, experimental evidence of magnetic coupled pendulums formed by controlled magnetic domain formation in square  $\text{Fe}_{70}\text{Co}_8\text{B}_{10}\text{Si}_{12}$  ferromagnetic elements is presented here. Static and dynamic magnetic properties of the full film and the patterned structures are investigated by inductive magnetometry and pulsed inductive microwave magnetometry [2], respectively. Magneto-optical Kerr microscopy [3] in the longitudinal mode is employed to characterize the magnetic domain structure.

As a prerequisite for the analysis of the patterned sample's behavior, the static and dynamic properties of an extended film were characterized. The hysteresis loops shown in

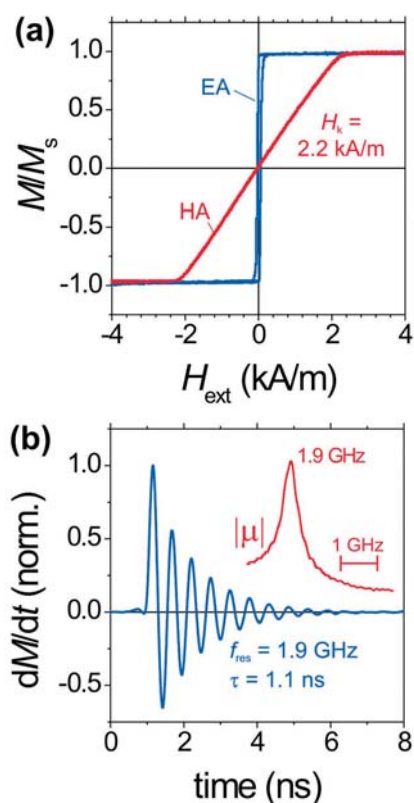


**Fig. 1: Static and dynamic full film magnetic properties.** (a) Magnetization loops along the easy axis (EA) and hard axis (HA) of magnetization for a single layer  $\text{Fe}_{70}\text{Co}_8\text{B}_{10}\text{Si}_{12}$  film with a thickness of 160 nm. The anisotropy field value  $H_k$  is indicated. (b) Normalized inductive signal  $U_{\text{ind}} \sim dM/dt$ . The inset in (b) shows the permeability amplitude spectrum  $|\mu|$  as derived from the time-domain data. The decay time  $\tau$  and the precessional frequency  $f_{\text{res}}$  of the damped oscillation, as well as the value of peak frequency of  $|\mu|$  are indicated.)

Fig. 1(a) display well pronounced easy axis (EA) and hard axis (HA) loop shapes with low coercivity values. An anisotropy field of  $H_k = 2.2$  kA/m is estimated from the HA magnetization loop. From the time-domain data of the magnetic response  $U_{\text{ind}} \sim dM/dt$  to a fast magnetic field step shown in Fig. 1(b) an oscillation frequency of  $f_{\text{res}} = 1.9$  GHz and a exponential decay time  $\tau = 1.1$  ns is derived. The time dependence of the change of magnetization is analogical to an underdamped oscillator. The magnetic permeability amplitude spectrum  $|\mu|$  displays one single peak.

With the patterning into an array of square elements, the static and dynamic magnetization response changes. The magnetization loops shown in Fig. 2(a) still display a noticeable difference in saturation field between the EA and HA direction. A representative magnetic domain image at  $H_{\text{ext}} = 0$  kA/m is displayed in the inset of Fig. 2(a). Due to the sufficiently high induced magnetic anisotropy of the deposited film, no Landau-like (hard axis) closure domains are generated at the edges. Instead, spike domains are formed at the edges to narrow the magnetic poles. In principle the domain structure can be described as a system with widely spaced domains in the central part of the element, which are limited by a band of narrowly spaced domains at the left and right side of the element. This bi-modal domain structure has a significant influence on the dynamic response as shown Fig. 2(b). In the time-domain signal, a clear indication of a beat known from coupling phenomena can be recognized. From the permeability spectrum, two peaks corresponding to two precessional frequency modes can be instantly identified. By comparing the time-domain signal with the full film data in Fig. 1(b), it becomes apparent that the decaying oscillation lasts longer for the element array relative to the extended film.

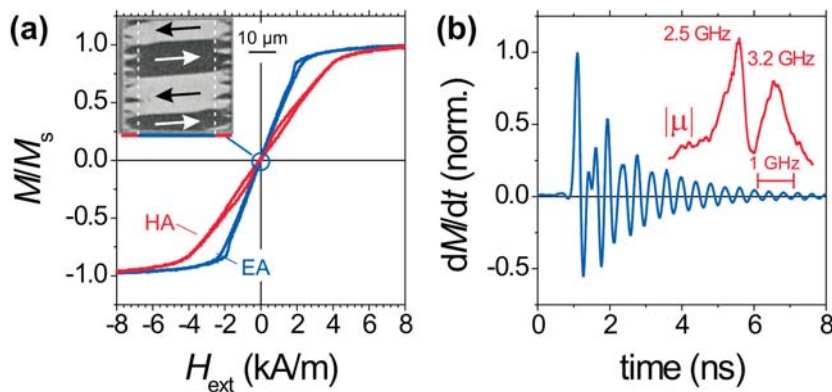


**Fig. 2: Static and dynamic properties of a single layer  $40 \mu\text{m} \times 40 \mu\text{m}$  element array.**

(a) Magnetization loops along EA and HA of magnetization. The magnetic domain structure of one representative element after applying a magnetic field along the EA is shown in the inset.

(b) Normalized change of magnetization  $dM/dt$  together with the corresponding decay time  $\tau$  and the precessional frequency  $f_{\text{res}}$ . The amplitude permeability spectrum  $|\mu|$  together with the values of the corresponding peak frequencies is shown in the inset of (b).

A quantitative evaluation of both precessional oscillations is shown in Fig. 3. A fit of the exponential decay of the precessional modes using just one fitting parameter for the average relaxation times results in a value of  $\tau = 2.2$  ns for the lower frequency mode at  $f_{\text{res}} = 2.4$  GHz (Fig. 3(a)), exceeding the extended film's decay time. The highly-damped high frequency mode, which we relate to the spike domain band at the edges, exhibits an average decay time of  $\tau = 0.7$  ns. The increase in  $f_{\text{res}}$  to 3.5 GHz and decrease in  $\tau$  is in

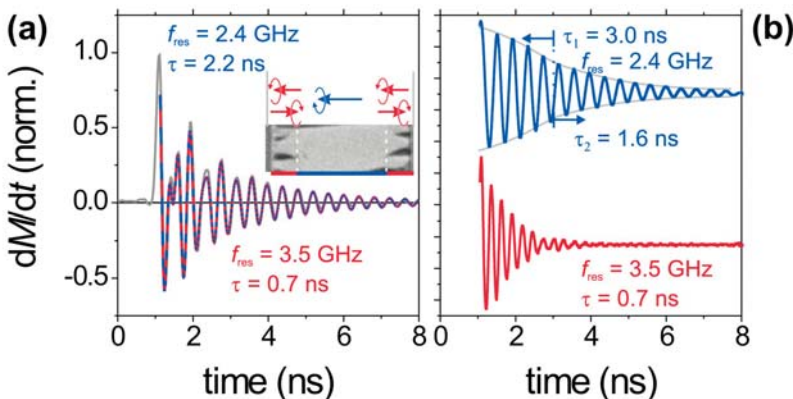
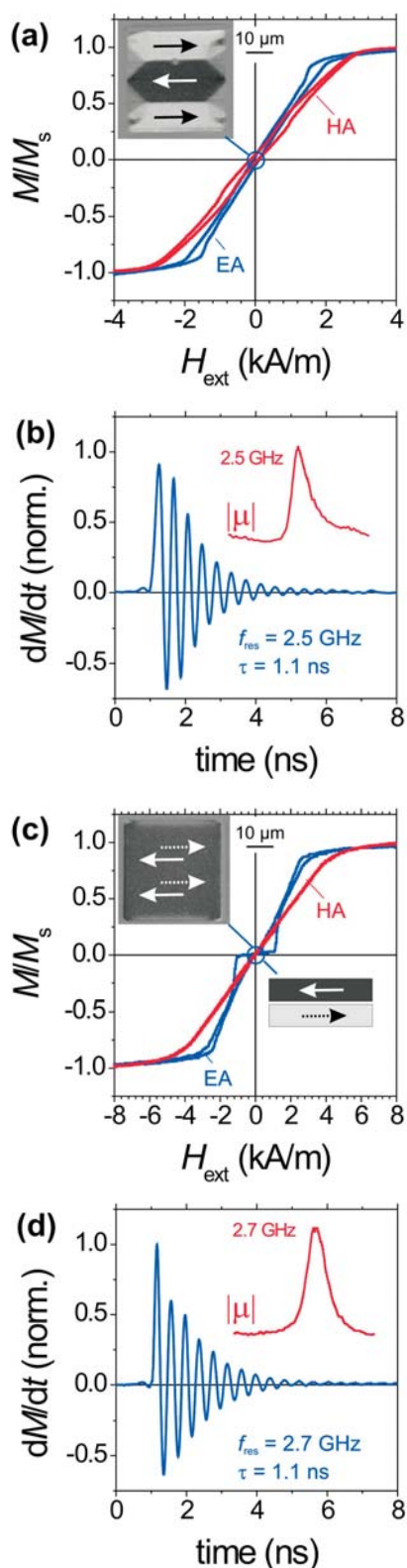


**Fig. 3: Analysis of the two precessional modes.**

(a) Measured bi-modal precession and fitted part of  $dM/dt$  above  $t \approx 1$  ns using only one decay time  $\tau$  for each precessional mode. The presumed location of the local excitation modes are sketched in the inset. (b) Analysis of the frequency response below and above  $f = 3$  GHz, respectively, as extracted from the time-domain signal by forward and selective backward Fourier transformation. The average decay times  $\tau$  and the precessional frequencies  $f_{\text{res}}$  of each mode are given.



agreement with our earlier results on the influence of domain wall spacing [2]. The assumed local distribution of the exhibited dynamic modes are displayed in the inset of Fig. 3(a). For a more detailed analysis of the magnetic response the data above  $t = 1$  ns was low- and high-pass filtered by forward and selective backward Fourier transformation with a cut-off frequency of 3 GHz. The results for the Fourier analysis of the magnetic response are displayed in Fig. 3(b). As can be seen from the sketched envelope of the low frequency response in Fig. 3(b), the use of a single decay time is just a crude estimate, as the initial decay is much smaller than for exceeding time. More realistic results are obtained by separately analyzing  $dM/dt$  below and above  $t = 3$  ns. From this, an initial average decay time of  $\tau_1 = 3.0$  ns and  $\tau_2 = 1.6$  ns for the subsequent relaxation is estimated. Evidently the system behaves similar to coupled pendulums, where energy is transferred from one magnetic oscillation mode into the other.

For verification of the made conclusion, two additional structures were investigated. First, the same structure was examined after a moderated HA anneal, which results in a reduced anisotropy field of  $H_k = 1.5$  kA/m (Fig. 4a). No other significant change in static magnetization loop shape relative to the original loop in Fig. 2(a) is seen. However, with the formation of a Landau-like domain structure as shown in Fig. 4(a), only one pronounced frequency  $f_{res} = 2.5$  GHz with a decay time of  $\tau = 1.1$  ns is exhibited (Fig. 4(b)). A small shoulder at higher frequencies is still visible in the permeability spectrum, which we attribute to the still existing small spike domains at the element's corners (Fig. 4(a)). Moreover, a laminated FeCoBSi/SiO<sub>2</sub>/FeCoBSi structure resulting in an anti-parallel alignment of magnetization in each layer, as indicated in Fig. 4(c), was investigated. For such structures no closure domains are formed and the system possesses only one single oscillation frequency. For both examples shown in Fig. 4, the average  $\tau$  is similar as for the extended full film case.

The complementary experiments undoubtedly proof that the exhibited bi-modal magnetic oscillation response is connected to the occurrence of a domain structure with two distinct regions of different domain wall density inside the magnetic elements. The amplification of the low-frequency signal results from energy transfer from the high-frequency dynamic mode into the low frequency mode. The observed transfer of magnetic energy from one region to another in magnetic elements adds a novel example to the phenomenon of coupled oscillators, as they are known in mechanics, electrodynamics, and various other examples in nature and physics.

**Fig. 4: Static and dynamic properties of alternative domain structures.**

(a) Magnetization loops along EA and HA of magnetization for a lower anisotropy structure together with magnetic domain structure at  $H_{ext} = 0$  kA/m. (b)  $dM/dt$  together with  $\tau$  and  $f_{res}$  and permeability spectrum  $|\mu|$ . (c) and (d) display the same, but for a FeCoBSi/SiO<sub>2</sub>/FeCoBSi (80nm/20nm/80nm) magnetic bi-layer structure with opposite alignment of magnetization as indicated in (c).

#### References

- [1] C. Back, D. Pescia, M. Buess, „Vortex dynamics”, in „Spin dynamics in confined magnetic structures III”, eds. B. Hillebrands and A. Thiaville, Springer Heidelberg-New York (2006)
- [2] U. Queitsch, J. McCord, A. Neudert, R. Schäfer, L. Schultz, K. Rott, H. Brückl: „Domain wall induced modes of high-frequency response in ferromagnetic elements”, *Journal of Applied Physics* 100, 093911 (2006)
- [3] A. Hubert and R. Schäfer, „Magnetic domains: The analysis of magnetic microstructures”, Springer Heidelberg-New York (1998)

## Magnetovolume effects in L1<sub>0</sub>-type FePt alloys

J. Lyubina, I. Opahle, M. Richter, O. Gutfleisch, K.-H. Müller, L. Schultz,  
O. Isnard (cooperation partner)

The dependence of the magnetic moments on the composition and chemical order in Fe-Pt alloys was studied by neutron powder diffraction. For alloys with almost perfect L1<sub>0</sub>-type long-range order, the experimental value of the Fe magnetic moment was determined to be  $2.8 \pm 0.1 \mu_B$  extrapolated to zero temperature. Combined analysis of experimental and density functional data shows that the Fe moment drops with increasing Fe content, which is primarily a consequence of the lattice volume reduction, whereas it is almost insensitive to the degree of order, in contrast to the well-known behavior of Fe-Al alloys.

FePt alloys have recently attracted considerable attention as candidates for ultrahigh-density magnetic storage media and as materials for special permanent magnet applications. The excellent magnetic properties of these alloys are associated with the ordered L1<sub>0</sub> FePt phase. Both experimental data and theoretical calculations indicate a correlation between the degree of order within the L1<sub>0</sub> phase and fundamental properties, such as magnetocrystalline anisotropy and Curie temperature. In contrast, the saturation magnetization of the L1<sub>0</sub> phase was reported to be largely independent of the degree of order at a fixed composition. The interpretation of the magnetization data is, however, complex and the data do not provide sufficient information about the individual atomic moments. Moreover, as the A1 to L1<sub>0</sub> transformation is of first order, a coexistence of both phases is frequently observed, which further complicates the analysis. Here, we report on a combined neutron powder diffraction and density functional study of ordered and partially ordered nanocrystalline Fe-Pt alloys. In particular, the dependence of atomic moments on the composition and the degree of long-range chemical order is investigated.

Fe-Pt alloys were prepared by mechanical ball milling and a subsequent heat treatment up to 930 K under vacuum, as described in more detail elsewhere [1]. The actual compositions of the reacted samples were determined by energy-dispersive x-ray (EDX) analysis in a scanning electron microscope to be Fe<sub>59</sub>Pt<sub>41</sub>, Fe<sub>48</sub>Pt<sub>52</sub>, and Fe<sub>50</sub>Pt<sub>50</sub>, respectively. The Fe<sub>50</sub>Pt<sub>50</sub> alloy was found to be essentially single L1<sub>0</sub> phase, as determined by x-ray diffraction. In Fe<sub>48</sub>Pt<sub>52</sub> and Fe<sub>59</sub>Pt<sub>41</sub>, along with the L1<sub>0</sub> phase, about 2 and 21 vol. % of the A1 phase was detected, respectively. The average crystallite size of the L1<sub>0</sub> phase is about 35 - 40 nm. Further analysis of the x-ray diffraction data shows that the L1<sub>0</sub> phase in the investigated alloys is well ordered, with order parameter close to the maximum value compatible with the respective composition: In Fe<sub>50</sub>Pt<sub>50</sub> and Fe<sub>48</sub>Pt<sub>52</sub>, almost all the Fe and Pt sites in L1<sub>0</sub> FePt are occupied by the correct atoms, while for Fe<sub>59</sub>Pt<sub>41</sub> a particular L1<sub>0</sub> structure is observed, with the Fe sites almost exclusively occupied by the correct atoms and about 20% of the Pt sites occupied by iron atoms.

Neutron powder diffraction patterns were recorded on the high-flux two-axis diffractometer D1B at the Institut Laue-Langevin. Figure 1 shows the evolution of the neutron diffraction patterns for the Fe<sub>50</sub>Pt<sub>50</sub> powder recorded during cooling from 920 K.

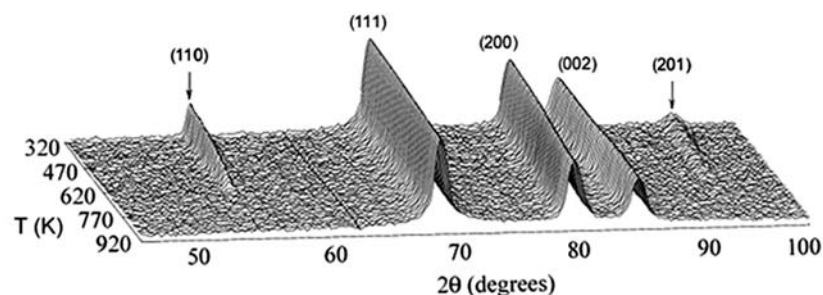


Fig. 1: Evolution of the neutron diffraction patterns with temperature for Fe<sub>50</sub>Pt<sub>50</sub> alloy. The diffraction peaks of the L1<sub>0</sub> FePt phase are marked, arrows indicate the position of the magnetic superstructure peaks.

At 920 K, only the fundamental (111), (200), and (002) diffraction peaks due to the  $L1_0$  phase are observed. As the temperature is lowered, the intensity of the fundamental reflections increases, and at about 725 K the (110) and (201) superstructure reflections are clearly observed. The intensity of these superstructure reflections is due to magnetic scattering only, since the intensities of the chemical superstructure peaks are negligible due to almost identical coherent neutron scattering lengths of Pt and Fe.

Magnetic structure refinement requires knowledge of the magnetic form factors of the elements. The Fe magnetic form factor used in our study is the one given in the International Tables for Crystallography. The magnetic form factor of Pt in ordered Fe-Pt alloys has not been precisely experimentally determined so far. However, exchange-enhanced paramagnetism is a well-known feature of Pt metal. Alloying Pt with, e.g., magnetic 3d transition metal elements induces a magnetic moment on Pt, which occurs due to the polarization of the Pt conduction electrons by the 3d electrons of the transition metal element and due to 3d-5d hybridization. Thus, we had to consider a possible contribution of the induced Pt magnetic moment to the neutron scattering. In the refinement, the Pt moment was set to  $0.3 \mu_B$ , while the Fe moments were not fixed. At room temperature, the magnetic moment of the Fe atoms in the  $L1_0$  phase amounts to about  $2.7 \mu_B$  in  $\text{Fe}_{50}\text{Pt}_{50}$ . It is somewhat reduced in the  $\text{Fe}_{48}\text{Pt}_{52}$  alloy and it is substantially reduced in  $\text{Fe}_{59}\text{Pt}_{41}$  by about 20%. For  $\text{Fe}_{59}\text{Pt}_{41}$  it was not possible to refine the magnetic moment of Fe on the Pt sites, and the observed moment is an average over all Fe atoms.

Fig. 2: Fe magnetic moment for  $\text{Fe}_{50}\text{Pt}_{50}$ ,  $\text{Fe}_{48}\text{Pt}_{52}$ , and  $\text{Fe}_{59}\text{Pt}_{41}$  in dependence on temperature, as obtained from neutron diffraction.

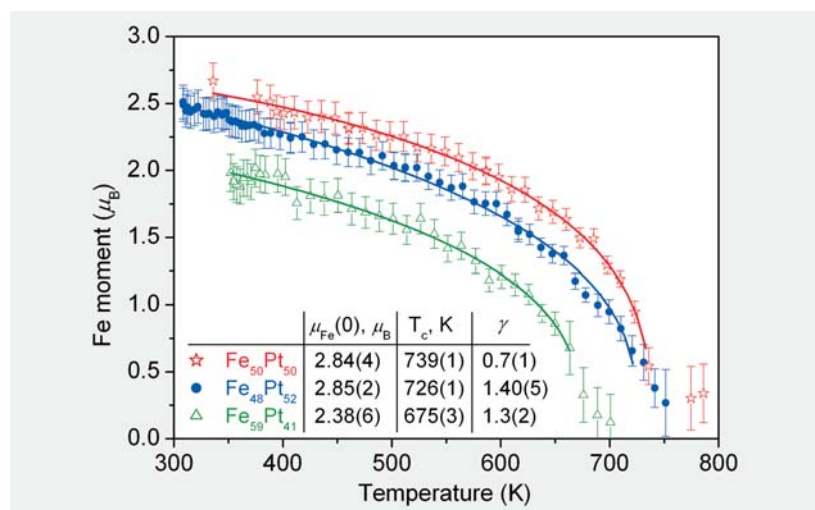


Figure 2 shows the thermal evolution of the magnetic moment of Fe obtained from the analysis of the neutron diffraction patterns collected during cooling. In order to evaluate the Fe moment at zero temperature, the temperature dependence of the Fe moment was fitted according to Ref. [2]. From the fit, the zero temperature moment of Fe was determined to be  $2.8 \mu_B$  for  $\text{Fe}_{50}\text{Pt}_{50}$  and  $\text{Fe}_{48}\text{Pt}_{52}$ , whereas for  $\text{Fe}_{59}\text{Pt}_{41}$  it is strongly reduced with a value of  $2.4 \mu_B$ . We estimated the total error to be  $\pm 0.1 \mu_B$ . The values of the Curie temperature obtained from the fit agree well with differential scanning calorimetry results and with literature data. The Curie temperature of the  $L1_0$  phase is very sensitive to the composition and, thus to the degree of order: it decreases from about 739 to 726 and to 675 K as the order parameter reduces from 0.99 to 0.97 and to 0.75. From the experimental data alone, it is difficult to judge whether disorder or the change in composition is the driving force behind the observed strong reduction of the Fe moment. Further insight is obtained from the results of our electronic structure calculations. The calculations were performed with the FPLO code [3] using the local spin density approximation (LSDA). Disorder was treated in the coherent potential approximation (CPA), with site occupations in accordance with the experimental values. Calculations

were performed for both the experimental lattice parameters and the theoretical LSDA volumes obtained by minimization of the total energy. During this minimization, the  $c/a$  ratios were kept fixed to the respective experimental value. The calculations reproduce the experimental dependence of the Fe moment on the composition. The calculated Fe moment of about  $2.85 \mu_B$  for the stoichiometric alloy  $\text{Fe}_{50}\text{Pt}_{50}$  agrees very well with the measured one. For the Pt-rich  $\text{Fe}_{48}\text{Pt}_{52}$  alloy, the small nonstoichiometry has only a minor influence on the iron moment. In the case of the iron rich  $\text{Fe}_{59}\text{Pt}_{41}$ , the calculations yield a substantial reduction of the Fe moment compared to the stoichiometric compound, in agreement with experiment. For the calculations performed at the experimental lattice parameters ( $M = 2.63 \mu_B$ ) this reduction is less pronounced than in the experiment, while the Fe moments calculated at the theoretical volume ( $M = 2.45 \mu_B$ ) are in almost perfect agreement with the measurements. Additional calculations at different lattice constants show that there is primarily one mechanism responsible for the smaller Fe moment in the Fe-rich compound: The smaller volume leads to a reduction of the moment, as is usual for itinerant magnets. Further contributions to this effect result from the change of the electronic structure with composition. Disorder in the lattice smoothens the density of states, which on the one hand side reduces the magnetic moments for fixed lattice parameters. However, on the other hand increasing disorder also leads to an increase of the volume, which in turn increases the magnetic moments. For more or less well ordered  $\text{Fe}_{59}\text{Pt}_{41}$  alloys both effects strongly compensate, and the iron moments are only weakly affected by a change of the order parameter for fixed composition. This behavior is in contrast to the Fe-Al system, where both disorder and increasing Fe content enhance the magnetism. In conclusion, the Fe moment in  $L1_0$ -type Fe-Pt alloys close to the stoichiometric composition is sensitive to composition and almost insensitive to the degree of order in the investigated range. The individual Fe and Pt moments decrease with increasing Fe content. Equiatomic well ordered Fe-Pt alloys are more suitable for hard magnetic applications, as they possess the highest Curie temperature.

## References

- [1] J. Lyubina, O. Isnard, I. Opahle, M. Richter, O. Gutfleisch, K.-H. Müller, L. Schultz: *Appl. Phys. Lett.*, **89** (2006) 032506.
- [2] M. D. Kuz'min: *Phys. Rev. Lett.* **94** (2005) 107204.
- [3] K. Koepf and H. Eschrig: *Phys. Rev. B* **59** (1999) 1743;  
see also <http://www.FPLO.de>.

**Cooperation** Laboratoire de Cristallographie, CNRS and Institut Laue-Langevin, Grenoble, France

**Funded by** DFG, SFB 463

## Breaking the isolated pentagon rule by chemical bonding: $\text{Sc}_3\text{N}@C_{70}$

S. Yang, A. Popov, L. Dunsch

The first  $C_{70}$ -based endohedral clusterfullerene -  $\text{Sc}_3\text{N}@C_{70}$  - was synthesized by the „reactive gas atmosphere” method and isolated by two-step HPLC. Based on the spectroscopic studies, the cage structure of  $\text{Sc}_3\text{N}@C_{70}$  has been elucidated by the combination of the experimental data and DFT computations, pointing out that this  $C_{70}$  cage is the  $C_{2v}$ :7854 isomer having three pairs of the adjacent pentagons, which is the first non-IPR isomer reported for  $C_{70}$ . The three pairs of the adjacent pentagons within  $\text{Sc}_3\text{N}@C_{70}$  ( $C_{2v}$ :7854) are coordinated to the three Sc atoms of the asymmetrical  $\text{Sc}_3\text{N}$  cluster. As a new example of stabilization of the non-IPR cages by a  $\text{Sc}_3\text{N}$  cluster,  $\text{Sc}_3\text{N}@C_{70}$  represents the fifth member of the non-IPR endohedral fullerene family.

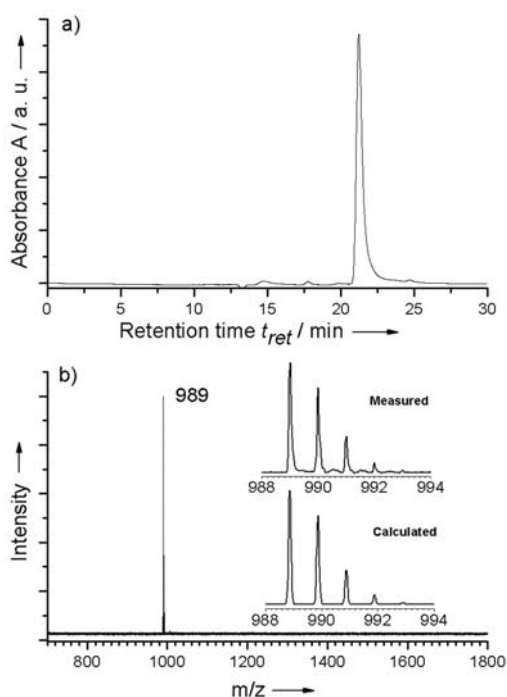


**Fig. 1:** a) Chromatogram of  $\text{Sc}_3\text{N}@C_{70}$  (10 x 250 mm Buckyclutcher column; flow rate 1.0 ml/min; injection volume 500  $\mu\text{l}$ ; toluene as eluent; 20°C). b) positive ion laser desorption time-of-flight (LD-TOF) mass spectrum of  $\text{Sc}_3\text{N}@C_{70}$ . The insets show the measured and calculated isotope distributions of  $\text{Sc}_3\text{N}@C_{70}$ .

Endohedral fullerenes as a novel form of fullerenes with atoms, ions, or clusters trapped in their inner space [1-5], exhibit a variety of new structural, magnetic and electronic properties which are important for the potential applications in electronics and medicine [1-7]. Recently many new endohedral fullerenes have been isolated with various encaged species as well as carbon cages. The latter have been demonstrated to exhibit a large variety in size ranging from  $C_{60}$  to  $C_{100}$  [1-12]. Even non-IPR (IPR=isolated pentagon rule) cages such as  $\text{Sc}_2@C_{66}$  [8],  $\text{Sc}_3\text{N}@C_{68}$  [9,11c],  $\text{Sc}_2\text{C}_2@C_{68}$  [13], and  $\text{La}_2@C_{72}$  [14] were isolated.  $C_{70}$ -based endohedral fullerenes appear to be quite peculiar because up to now only few non-metal atoms such as He (Ne, Ar, Kr, Xe) [15], N [16] and P [16a] were reported to be encapsulated inside the  $C_{70}$  cage. The metal atoms, which regularly form endohedral fullerenes with other cages [1-12], have never been entrapped in  $C_{70}$ . In addition to  $\text{Sc}_3\text{N}@C_{68}$ , the trimetallic nitride endohedral fullerenes (clusterfullerenes) give rise to a large variation of the cage sizes [3,5,11,12], but the  $C_{70}$  cage was missed. Herein we report the synthesis of the first  $C_{70}$ -based endohedral clusterfullerenes  $\text{Sc}_3\text{N}@C_{70}$  by the „reactive gas atmosphere” method and its structural elucidation.

$\text{Sc}_3\text{N}@C_{70}$  is synthesized by the „reactive gas atmosphere” method along with several known  $\text{Sc}_3\text{N}@C_{2n}$  ( $2n = 68, 78, 80$ ) clusterfullerenes [3,5,11c,12a]. The isolation of  $\text{Sc}_3\text{N}@C_{70}$  was accomplished by two-step HPLC. Briefly, in the first-step HPLC running on a Buckyprep column,  $\text{Sc}_3\text{N}@C_{70}$  was eluted together with  $C_{84}$ , which was consequently removed in the second-step HPLC performed on a Buckyclutcher column. The  $\geq 99\%$  purity of the isolated  $\text{Sc}_3\text{N}@C_{70}$  ( $t_{\text{ret}} = 21.5$  min,  $m/z = 989$ ) resulted from the successful isolation is ascertained by both the HPLC and MS analysis as shown in Figure 1. The good agreement of the measured isotope distribution of  $\text{Sc}_3\text{N}@C_{70}$  with the calculated one confirms the proposed composition (see inset of Figure 1b). The yield of  $\text{Sc}_3\text{N}@C_{70}$  is only about 1.8% of that of  $\text{Sc}_3\text{N}@C_{68}$ .

The UV-vis-NIR spectrum of  $\text{Sc}_3\text{N}@C_{70}$  dissolved in toluene is shown in Figure 2. Based on the absorption spectral onset of ca. 960 nm, the optical band-gap of  $\text{Sc}_3\text{N}@C_{70}$  is estimated to be 1.3 eV [1-12], indicating that  $\text{Sc}_3\text{N}@C_{70}$  is a large band-gap and hence a stable fullerene. The optical band-gap of  $\text{Sc}_3\text{N}@C_{70}$  is larger than those of  $\text{Sc}_3\text{N}@C_{68}$  (1.1 eV) and  $\text{Sc}_3\text{N}@C_{78}$  (1.0 eV) but smaller than those of  $\text{Sc}_3\text{N}@C_{80}$  (I) (1.7 eV) and  $\text{Sc}_3\text{N}@C_{80}$  (II) (1.6 eV) [9,11c,12a,19]. The electronic absorption spectrum of  $\text{Sc}_3\text{N}@C_{70}$  is less rich in features than that of its neighboring clusterfullerene  $\text{Sc}_3\text{N}@C_{68}$  [11c]. The strongest absorption of  $\text{Sc}_3\text{N}@C_{70}$  lies at 696 nm along with several shoulder peaks at 468, 558, 807, and 894 nm (see inset of Figure 2), which are in general red-shifted compared to

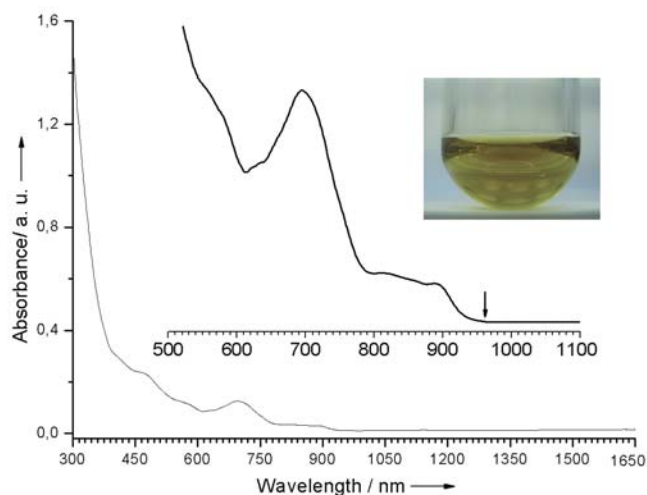


**Fig. 2:** UV-Vis-NIR spectrum of  $\text{Sc}_3\text{N}@C_{70}$  dissolved in toluene. The insets show the enlarged spectral range (500–1100 nm) and the photograph of  $\text{Sc}_3\text{N}@C_{70}$  dissolved in toluene. The arrow labels the spectral onset.

$\text{Sc}_3\text{N}@C_{68}$  [11c]. Accordingly, the color of  $\text{Sc}_3\text{N}@C_{70}$  dissolved in toluene (green-yellow, see inset of Figure 2) is quite different to that of  $\text{Sc}_3\text{N}@C_{68}$  (purple) as well as  $\text{Sc}_3\text{N}@C_{78}$  (dark green) and  $\text{Sc}_3\text{N}@C_{80}$  (I) (orange).

Figure 3 presents the FTIR spectrum of  $\text{Sc}_3\text{N}@C_{70}$  (curve a), exhibiting significant differences from those of  $\text{Sc}_3\text{N}@C_{68}$  ( $D_3$ ),  $\text{Sc}_3\text{N}@C_{78}$  ( $D_{3h}$ ) and  $\text{Sc}_3\text{N}@C_{80}$  (I,  $I_h$ ) and (II,  $D_{5h}$ ) reported before by our group [3,5,11c,12a,12e]. Compared to  $\text{Sc}_3\text{N}@C_{80}$  (I, II) [12a], the spectrum of  $\text{Sc}_3\text{N}@C_{70}$  exhibits a relatively larger number of lines, suggesting a low cage symmetry of  $\text{Sc}_3\text{N}@C_{70}$ . Note that the overall spectral pattern of  $\text{Sc}_3\text{N}@C_{2n}$  clusterfullerenes, which is mostly contributed from the tangential and radial cage modes [3,5,11c,12a,12e,20], is highly sensitive to the structure of the fullerene. Thus, such a high structural sensitivity enables infrared (IR) spectroscopy to be a powerful tool for the structural analysis of the clusterfullerenes [3–5,11–12,20].

To elucidate the cage symmetry of  $\text{Sc}_3\text{N}@C_{70}$ , IPR-obeying  $D_{5h}$  cage (isomer 8149) was firstly considered, and its molecular structure and IR spectrum were calculated at the DFT level. Obviously the computed IR spectrum of  $\text{Sc}_3\text{N}@C_{70}$  ( $D_{5h}$ : 8149) (curve c in Figure 3) does not fit the experimental spectrum. In addition, the DFT-calculated HOMO-LUMO gap of  $\text{Sc}_3\text{N}@C_{70}$  ( $D_{5h}$ : 8149) is only 0.53 eV, which is substantially smaller than the measured value [21]. Thus, for  $\text{Sc}_3\text{N}@C_{70}$  both the HOMO-LUMO gap and the IR spectrum rule out the IPR-obeying  $D_{5h}$  cage (isomer 8149). Hence an appropriate non-IPR cage (out of 8148 non-IPR isomers of  $C_{70}$  [22]) must be considered as the cage structure of  $\text{Sc}_3\text{N}@C_{70}$ .

As IPR disfavors fullerene isomers with edge-sharing pentagons due to the increased local strain for the carbon atoms on the shared edges, it is justified for the non-charged carbon cages with an amount of p-electrons coinciding with the number of carbon atoms [22]. The driving force of the formation of  $\text{Sc}_3\text{N}$ -encapsulating clusterfullerenes is the formal transfer of six electrons from the cluster to the lowest unoccupied molecular orbitals (LUMO) of the fullerene [11c,12e,23]. Thus, up to 6 carbon atoms in the 6-fold charged cages may formally have  $sp^3$  hybridization causing a violation of the IPR rule. Encapsulation of a metal or cluster may result in an additional stabilization of formally  $sp^3$ -hybridized carbon atoms [8,9,11c,13,14] and thus non-IPR cages become stable as already demonstrated for the reported four non-IPR structures [24]. Hence, it is reasonable to assume that the cage hosting  $\text{Sc}_3\text{N}$  should have no more than three pairs of edge-sharing pentagons, which should be located on the cage in such a way that their coordinations with the Sc atoms of the cluster are possible.

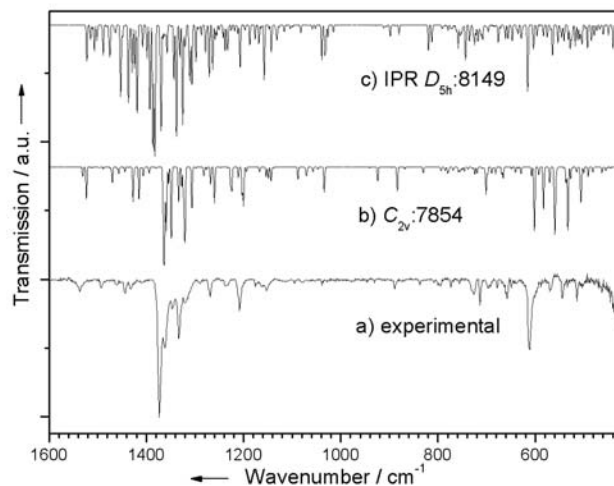


**Fig. 3:** Experimental FTIR spectrum of  $\text{Sc}_3\text{N}@C_{70}$  (a) and calculated IR spectra of the non-IPR isomer of  $C_{2v}$ :7854  $\text{Sc}_3\text{N}@C_{70}$  (b), IPR-obeyed isomer of  $\text{Sc}_3\text{N}@C_{70}$   $D_{5h}$ :8149 (c).

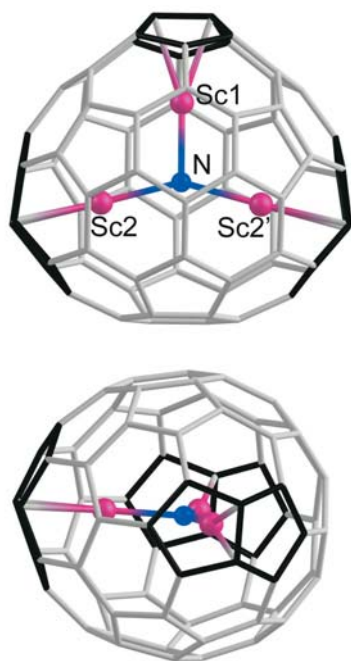


Fig. 4: DFT-optimized structure of  $\text{Sc}_3\text{N}@C_{70}$  ( $C_{2v}$ :7854). Three pairs of the adjacent pentagons are highlighted in black.

Using the above criteria, 116 isomers with three or less pairs of adjacent pentagons are to be preferably considered among 8148 non-IPR isomers of  $C_{70}$ . For all these isomers we have performed DFT optimization of the hexaanions [25]. It is found that for the 6-fold charged state the isomer  $C_{2v}$ :7854 has the highest HOMO-LUMO gap (1.24 eV) and is the most stable one (ca. 43 kJ/mol lower in energy than that of  $D_{5h}$ :8149) [26]. This isomer is the only one in the whole set of the 116 isomers which has a HOMO-LUMO gap above 1 eV.

Encapsulation of the  $\text{Sc}_3\text{N}$  cluster results in an additional stabilization of the  $C_{2v}$ :7854 cage. According to DFT calculation,  $\text{Sc}_3\text{N}@C_{70}$  ( $C_{2v}$ :7854) (Figure 4) is 164 kJ/mol more stable in energy than  $\text{Sc}_3\text{N}@C_{70}$  ( $D_{5h}$ :8149). The calculated HOMO-LUMO gap of  $\text{Sc}_3\text{N}@C_{70}$  ( $C_{2v}$ :7854) is 1.29 eV, almost the same as for the hexaanion of empty  $C_{70}$ . Following the location of the adjacent pentagons, the  $\text{Sc}_3\text{N}$  cluster has a  $C_{2v}$  symmetry and is significantly distorted from the equilateral triangle configuration. DFT optimized Sc1-N-Sc2 and Sc2-N-Sc2' angles are  $105^\circ$  and  $150^\circ$ , respectively, while Sc1-N and Sc2-N bond lengths are 1.987 and 2.060 Å, respectively.

The DFT-simulated IR spectrum of  $\text{Sc}_3\text{N}@C_{70}$  ( $C_{2v}$ :7854) is compared to the experimental one (Figure 3). Unlike for  $\text{Sc}_3\text{N}@C_{70}$  ( $D_{5h}$ :8149), a perfect agreement of the computed spectrum (curve b, Figure 3) with the experimental one (curve a, Figure 3) is observed for  $\text{Sc}_3\text{N}@C_{70}$  ( $C_{2v}$ :7854) in the ranges of both the tangential and radial cage modes [27]. Therefore, based on both the analysis on the HOMO-LUMO gap and the IR spectrum, the isomer  $C_{70}$  ( $C_{2v}$ :7854) is assigned as the cage structure of  $\text{Sc}_3\text{N}@C_{70}$  [28].

In summary, we have successfully synthesized the first non-IPR  $C_{70}$ -cage hosting an endohedral cluster:  $\text{Sc}_3\text{N}@C_{70}$ . This non-IPR  $\text{Sc}_3\text{N}@C_{70}$  is a stable fullerene with a large band-gap of 1.3 eV as revealed by UV-vis-NIR spectroscopy. FTIR spectroscopic study in combination with DFT calculation accomplishes the assignment of the non-IPR  $C_{2v}$ :7854 isomer as the cage structure of  $\text{Sc}_3\text{N}@C_{70}$ . Thus, besides  $\text{Sc}_3\text{N}@C_{68}$ ,  $\text{Sc}_3\text{N}@C_{70}$  provides a further example of stabilization of the non-IPR cages by encapsulation of an asymmetrical  $\text{Sc}_3\text{N}$  cluster, which is different to all other reported symmetrical  $\text{Sc}_3\text{N}$ -based clusterfullerenes. With  $\text{Sc}_3\text{N}@C_{70}$  representing the fifth member of the non-IPR endohedral fullerene family, this study opens up new insight into the non-IPR feature of endohedral fullerenes.

## References

- [1] L. Dunsch, S. Yang: *Electrochem. Soc. Interface* **15**(2) (2006) 34.
- [2] a) H. Shinohara: *Rep. Prog. Phys.* **63** (2000) 843. b) *Endofullerenes: A New Family of Carbon Cluster* (Eds.: T. Akasaka, S. Nagase), Kluwer Academic Publishers, Dordrecht, 2002.
- [3] L. Dunsch, M. Krause, J. Noack, P. Georgi, *J. Phys. Chem. Sol.* **65** (2004) 309.
- [4] S. F. Yang, L. Dunsch, *Angew. Chem.* **118** (2006) 1321; *Angew. Chem. Int. Ed.* **45** (2006) 1299.
- [5] For a recent invited review, see L. Dunsch, S. Yang, *Small* (2007) submitted.
- [6] S. H. Yang, *Trends in Chem. Phys.* **9** (2001) 31.
- [7] S. F. Yang, L. Z. Fan, S. H. Yang, *J. Phys. Chem. B* **108** (2004) 4394.
- [8] C. R. Wang, T. Kai, T. Tomiyama, T. Yoshida, Y. Kobayashi, E. Nishibori, M. Takata, M. Sakata, H. Shinohara, *Nature* **408** (2000) 426.
- [9] S. Stevenson, P. W. Fowler, T. Heine, J. C. Duchamp, G. Rice, T. Glass, K. Harich, E. Hajdu, R. Bible, H. C. Dorn, *Nature* **408** (2000) 427.
- [10] C. R. Wang, T. Kai, T. Tomiyama, T. Yoshida, Y. Kobayashi, E. Nishibori, M. Takata, M. Sakata, H. Shinohara, *Angew. Chem.* **113** (2001) 411; *Angew. Chem. Int. Ed.* **40** (2001) 397.

- [11] a) S. F. Yang, L. Dunsch, *J. Phys. Chem. B* **109** (2005) 12320; b) S. F. Yang, L. Dunsch, *Chem. Eur. J.* **12** (2006) 413; c) S. F. Yang, M. Kalbac, A. Popov, L. Dunsch, *Chem. Eur. J.* **12** (2006) 7856; d) S. F. Yang, M. Kalbac, A. Popov, L. Dunsch, *ChemPhysChem* **7** (2006) 1990; e) S. F. Yang, S. Troyanov, A. Popov, M. Krause, L. Dunsch, *J. Am. Chem. Soc.* **128** (2006) 16733.
- [12] a) M. Krause, L. Dunsch, *ChemPhysChem* **5** (2004) 1445; b) M. Krause, J. Wong, L. Dunsch, *Chem. Eur. J.* **11** (2005) 706; c) M. Krause, L. Dunsch, *Angew. Chem.* **117** (2005) 1581; *Angew. Chem. Int. Ed.* **44** (2005) 1557; d) M. Krause, X. Liu, J. Wong, T. Pichler, M. Knupfer, L. Dunsch, *J. Phys. Chem. A* **109** (2005) 7088; e) M. Krause, A. Popov, L. Dunsch, *ChemPhysChem* **7** (2006) 1734.
- [13] Z. Q. Shi, X. Wu, C. R. Wang, X. Lu, H. Shinohara, *Angew. Chem.* **118** (2006) 2161; *Angew. Chem. Int. Ed.* **45** (2006) 2107.
- [14] a) H. Kato, A. Taninaka, T. Sugai, H. Shinohara, *J. Am. Chem. Soc.* **125** (2003) 7782; b) C. M. Beavers; T. Zuo, J. C. Duchamp, K. Harich, H. C. Dorn, M. M. Olmstead, A. L. Balch, *J. Am. Chem. Soc.* **128** (2006) 11352.
- [15] a) M. Saunders, H. A. Jimenezvaquez, R. J. Cross, S. Mroczkowski, D. I. Freedberg, F. A. L. Anet, *Nature* **367** (1994) 256; b) M. Saunders, H. A. Jimenezvaquez, R. J. Cross, S. Mroczkowski, M. L. Cross, D. E. Giblin, R. J. Poreda, *J. Am. Chem. Soc.* **116** (1994) 2193.
- [16] a) E. Dietel, A. Hirsch, B. Pietzak, M. Waiblinger, K. Lips, A. Weidinger, A. Gruss, K. P. Dinse, *J. Am. Chem. Soc.* **121** (1999) 2432; b) K. Lips, M. Waiblinger, B. Pietzak, A. Weidinger, *Molecular Materials* **13** (2000) 217.
- [17] S. Stevenson, G. Rice, T. Glass, K. Harich, F. Cromer, M.R. Jordan, J. Craft, E. Hajdu, R. Bible, M. M. Olmstead, K. Maitra, A.J. Fisher, A.L. Balch, H.C. Dorn, *Nature* **401** (1999) , 55.
- [18] L. Dunsch, P. Georgi, M. Krause, C. R. Wang, *Synth. Met.* **135** (2003) 761.
- [19] M. M. Olmstead, A. Bettencourt-Dias, J. C. Duchamp, S. Stevenson, D. Marciu, H. C. Dorn, A. L. Balch, *Angew. Chem.* **113** (2001) 1263; *Angew. Chem. Int. Ed.* **40** (2001) 1223.
- [20] M. Krause, H. Kuzmany, P. Georgi, L. Dunsch, K. Vietze, G. Seifert, *J. Chem. Phys.* **115** (2001) 6596.
- [21] It is well known that DFT systematically underestimates the HOMO-LUMO gap, but for  $\text{Sc}_3\text{N}@C_{68}$  and  $\text{Sc}_3\text{N}@C_{78}$  the code that we used yielded an underestimation of only 0.2 eV (see refs. [11c,12e]). Considering a comparable underestimation or even a higher value of up to 0.5 eV for  $\text{Sc}_3\text{N}@C_{70}$ , the predicted HOMO-LUMO gap is still less than 1 eV and therefore much smaller than the measured one (1.3 eV).
- [22] Since the number of non-IPR isomers of  $C_{70}$  (8148, see P. W. Fowler, D. E. Manolopoulos, *An Atlas of Fullerenes*, Clarendon Press, Oxford, 1995.) is very high, it is necessary to establish some criteria in order to exclude those non-IPR cages, which are highly strained and unfavorable, and consequently to reduce the set of probable structures.
- [23] J. M. Campanera, C. Bo, J. M. Poblet, *Angew. Chem.* **117** (2005) 7396; *Angew. Chem. Int. Ed.* **44** (2005) 7230.
- [24] These include  $\text{Sc}_2@C_{66}$ ,  $\text{Sc}_3\text{N}@C_{68}$ ,  $\text{Sc}_2\text{C}_2@C_{68}$  and  $\text{La}_2@C_{72}$ . Note that in all these cases the pairs of adjacent pentagons are coordinated to the endohedral metal atoms.
- [25] Since in trimetallic nitride clusterfullerenes six electrons of the cluster are formally transferred to the carbon cage, the analysis of the relative energies and HOMO-LUMO gaps in hexaanions (rather than in the neutrally charged isomers) is reasonable (see also refs. [11c,12e,22]).
- [26] Note that in the neutral form  $C_{2v}:7854$  isomer of  $C_{70}$  is 369 kJ/mol less stable than IPR-obeyed isomer of  $C_{70}$  ( $D_{5h}$ :8149).
- [27] Similar good agreements of the DFT-simulated IR spectra with the measured ones have been revealed for the cases of  $\text{Sc}_3\text{N}@C_{68}$  ( $D_3$ ) and  $\text{Sc}_3\text{N}@C_{78}$  ( $D_{3h}$ ), for which the systematic underestimation of the computed frequencies by ca  $10\text{ cm}^{-1}$  was already documented for our DFT code (see refs. [11c,12e]), justifying the reliability of the code used for DFT calculations and confirming the assignment of the cage structure by this method.
- [28] S. F. Yang, A. Popov, L. Dunsch, *Angew. Chem. Int. Ed.* **46** (2007) 1256

## Amorphous-nanocrystalline Mg-Ni-Y alloys for room temperature hydrogen storage

A. Gebert, A. Teresiak, B. Khorkounov, J. Thomas, C. Mickel, M. Uhlemann, J. Eckert, L. Schultz

Glass-forming Mg-Ni-Y alloys prepared by mechanical alloying and rapid quenching were investigated regarding their suitability as hydrogen absorbing cathode materials for rechargeable Ni-MH<sub>x</sub> batteries. Electrochemically charged hydrogen influences the thermal crystallization process by hydride formation Mg<sub>2-x</sub>Ni<sub>1-y</sub>Y<sub>x+y</sub>H<sub>z</sub> and inhibition of the appearance of the new metastable Mg<sub>6</sub>Ni phase. Electrodes made from alloy powders with nanocrystalline-amorphous structure and with optimised design exhibit substantially enhanced maximum discharge capacities. Surface reactions during charge-discharge cycling in the strongly alkaline battery electrolyte are analysed in detail.

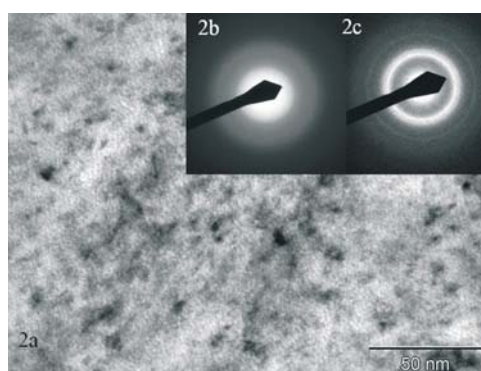


**Fig. 1:** TEM bright field image (a) and electron diffraction patterns of amorphous (b) and nanocrystalline (c) regions of rapidly quenched Mg<sub>77</sub>Ni<sub>18</sub>Y<sub>5</sub>.

In the development of new cathode materials of rechargeable Ni-MH<sub>x</sub> batteries [1] Mg-Ni-based alloys, closely related to the Mg<sub>2</sub>Ni compound with a theoretical discharge capacity C<sub>max</sub> = 1000 mAh/g (~ Mg<sub>2</sub>NiH<sub>4</sub> with 3,6 wt.% hydrogen) [2], find currently special attention. However, measured discharge capacities and cycle lifes of electrodes made from microcrystalline Mg<sub>2</sub>Ni are very low, mainly due to a slow hydriding kinetics caused by blocking hydride layers on the grain surfaces and to severe corrosion processes during cycling. Microstructural refinements and compositional changes are essential to improve the electrode performance. The reported C<sub>max</sub> values of electrodes made from mechanically alloyed nanocrystalline Mg<sub>2</sub>Ni powders vary from 100 to 200 mAh/g [3]. Compositional modifications with transition metals, e.g. Ti and Zr [4], or rare earths [5] are considered as most useful ways for improving the cycle life. Metastable Mg-Ni-Y alloys with high glass-forming ability, which crystallize under formation of Mg<sub>2</sub>Ni, are considered as promising candidates for those hydrogen storage applications. Selected alloys prepared by rapid quenching and mechanical alloying are fundamentally investigated regarding the effect of hydrogen on the phase stability and thermal phase transformations as well as regarding their electrochemical hydrogen charge - discharge behaviour in strongly alkaline electrolyte.

In-situ high temperature X-ray diffraction is an excellent tool to observe phase formation and transformation processes of metastable Mg-based alloys directly at elevated temperatures in defined time windows and varying gaseous atmospheres. By means of this advanced technique rapidly quenched Mg<sub>77</sub>Ni<sub>18</sub>Y<sub>5</sub> samples in different hydrogen pre-charged states were investigated [6]. The as-quenched alloy exhibits an amorphous-nanocrystalline microstructure as shown in the TEM bright-field image (Fig. 1a)

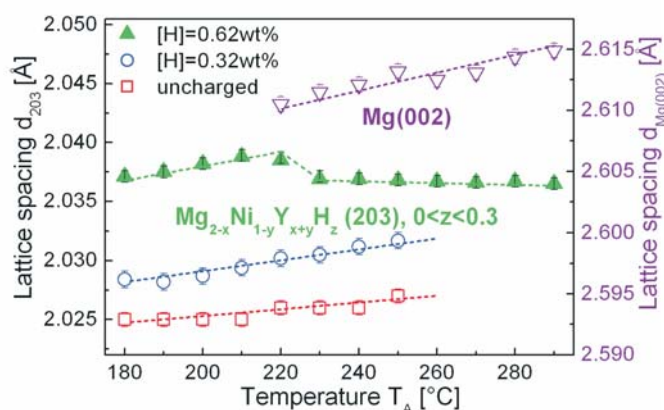


**Fig. 2:** Change of lattice spacing  $d_{(203)}$  of Mg<sub>2-x</sub>Ni<sub>1-y</sub>Y<sub>x+y</sub>H<sub>z</sub> during heating of Mg<sub>77</sub>Ni<sub>18</sub>Y<sub>5</sub> with different hydrogen contents.

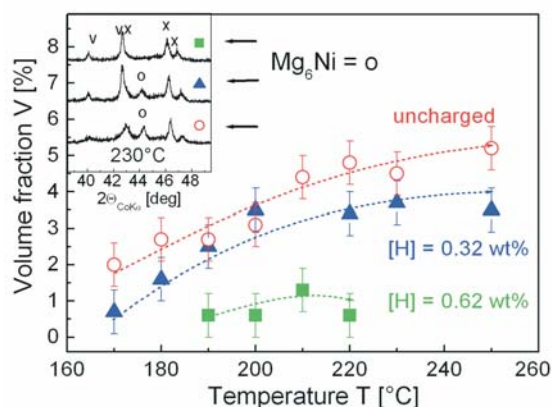


**Fig. 3:** Change of volume fraction of Mg<sub>6</sub>Ni during heating of Mg<sub>77</sub>Ni<sub>18</sub>Y<sub>5</sub> with different hydrogen contents.

with selected area electron diffraction patterns (Fig. 1b + c). The nanocrystals with 2–8 nm size consist of a solid solution of hexagonal  $Mg_2Ni$  and Y,  $Mg_{2-x}Ni_{1-y}Y_{x+y}$ . After electrochemical pre-charging at room temperature up to a hydrogen content of  $[H]=0.62$  wt.% no significant change in the microstructure was evidenced, while higher contents up to  $[H]=1.42$  wt.% lead to the formation of a second phase. Upon heating under high vacuum conditions the as-quenched alloy is firstly subjected to crystallisation of  $Mg_{2-x}Ni_{1-y}Y_{x+y}$  and grain growth starting at  $T=130^\circ C$ . Yttrium leaves this phase slowly at  $250 < T < 300^\circ C$ . With increasing hydrogen content and temperature, in the XRD patterns a clear  $2\theta$  peak-shift of the  $Mg_{2-x}Ni_{1-y}Y_{x+y}$  phase is observed corresponding to a significant lattice expansion (Fig. 2). This indicates that a part of the hydrogen is interstitially dissolved in this phase leading to  $Mg_{2-x}Ni_{1-y}Y_{x+y}H_z$ , while the residual hydrogen is mainly located in the grain boundaries and inhibits the crystal growth. The desorption of hydrogen from this phase starts above  $220^\circ C$  for  $[H]=0.62$  wt.%, as can be seen in Fig. 2 from a drop of the d-values (203), and at  $250^\circ C$  for  $[H]=0.32$  wt%. Besides the  $Mg_{2-x}Ni_{1-y}Y_{x+y}$  phase, during the crystallisation of rapidly quenched  $Mg_{77}Ni_{18}Y_5$  the formation of the metastable  $Mg_6Ni$  phase is observed at  $T > 160^\circ C$ , which decomposes to into  $Mg_2Ni$  and Mg at  $T > 250^\circ C$ . This phase was similarly detected during crystallisation of other Mg–Ni–Y alloys [7]. With increasing pre-charged hydrogen content in the alloy the volume fraction of this phase decreases and its existence region diminishes (Fig. 3) suggesting a very low reactivity of  $Mg_6Ni$  with hydrogen. For a better understanding of the phase reactions, the  $Mg_{85.7}Ni_{14.3}$  alloy corresponding to single-phase  $Mg_6Ni$  was prepared by melt spinning. The thermal behaviour was studied with regard to the refinement of the crystal structure and the behaviour under hydrogen atmosphere [8]. The as-quenched alloy has an amorphous-nanocrystalline structure with nanocrystals of 2–5-nm size. Under He atmosphere the crystallisation of  $Mg_6Ni$  starts at  $140^\circ C$  and above  $230^\circ C$  it decomposes into Mg and  $Mg_2Ni$ . From the completely crystallised  $Mg_6Ni$  phase the HR-TEM image and the well defined electron diffraction pattern shown in Fig. 4 were gained. The cubic complex  $Mg_{340.04}Pd_{55.84}$  structure (F-43m [9]) was fitted by replacing the Pd atoms by Ni atoms (Fig. 5). Additionally, the structure refinement of XRD patterns confirmed the structure type and yielded an average lattice constant of  $a = 20.043 \pm 0.002 \text{ \AA}$ . By electrochemical charging the alloy absorbs only insignificant amounts of hydrogen. Isothermal heat treatments were performed in a 0.5 MPa hydrogen atmosphere at  $T = 120^\circ C$ . Hot gas extraction of the sample revealed a hydrogen content of  $[H] = 0.34$  wt.% indicating that also under these conditions an interstitial absorption of hydrogen in the  $Mg_6Ni$  cell does not occur. The hydrogen is located in the grain boundaries and thus, inhibits the crystal growth and initiates the decomposition of the  $Mg_6Ni$  phase at lower temperatures.

$Mg_{63}Ni_{30}Y_7$  alloy samples were subjected to electrochemical studies to evaluate their hydride electrode performance. The XRD patterns of mechanically alloyed powders (Fig. 6) reveal a strong influence of the milling conditions on the phase formation process. Milling of elemental powders in a Retsch planetary ball mill under liquid nitrogen leads to a main amorphous phase. But milling in a SPEX shaker mill at ambient temperature results in a nanocrystalline hexagonal  $Mg_2Ni$  main phase with Y being alloyed into this phase, i.e.  $Mg_{2-x}Ni_{1-y}Y_{x+y}$ . TEM studies (Fig. 7) identified for the Retsch-milled material besides the main amorphous phase also a few nanocrystals (3–60 nm) and for the SPEX-milled material a nanocrystalline structure ( $< 100$  nm) and also small amorphous fractions [10]. The powders were used for the preparation of metal hydride electrodes by mixing them with nickel powder and PVA and pressing this mixture onto a nickel foam. Those electrodes were tested in a 6 M KOH battery electrolyte with  $pH = 14.8$  at room temperature [10]. Fig. 7 summarizes results of galvanostatic charge-discharge cycling tests, i.e. discharge curves of the cycle with the maximum discharge capacity  $C_{max}$ . For electrodes with SPEX-milled powder a  $C_{max} = 247$  mAh/g is reached in the 2. cycle. The electrodes made from Retsch-milled powder require a longer activation procedure: a

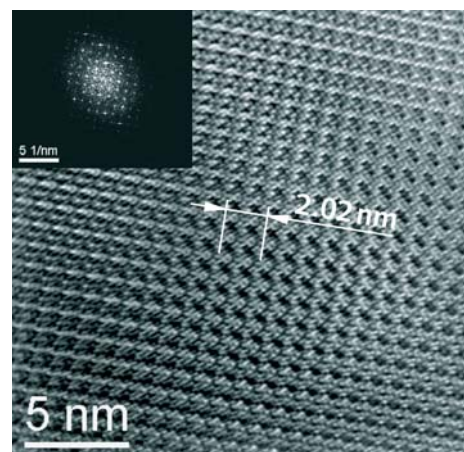


Fig. 4: HR-TEM image and electron diffraction pattern of  $Mg_6Ni$ , unit cell [100]-direction.

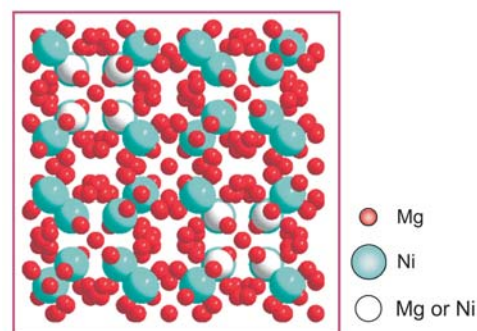


Fig. 5:  $Mg_6Ni$  complex structure.

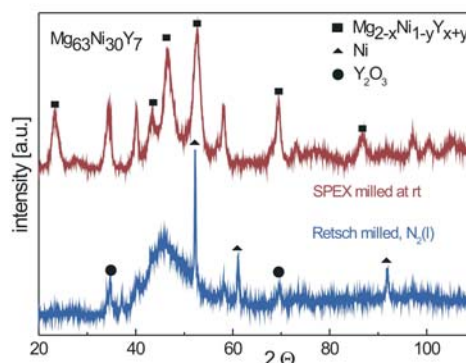
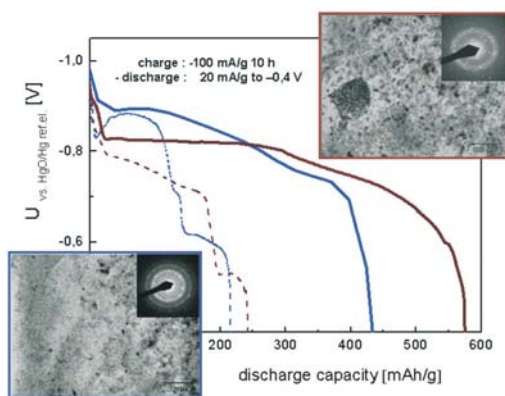
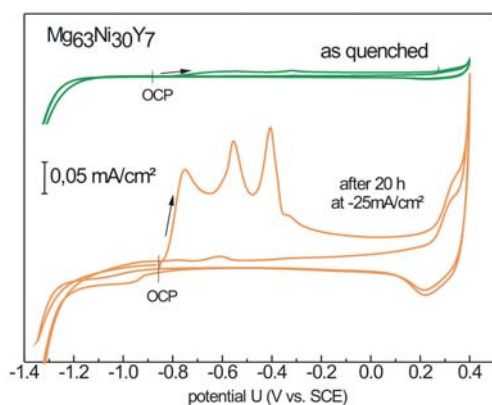


Fig. 6: XRD patterns of mechanically alloyed  $Mg_{63}Ni_{30}Y_7$  powders, influence of milling conditions.



**Fig. 7:** Maximum discharge curves of electrodes made from  $Mg_{63}Ni_{30}Y_7$  powders: - - - + Ni on Ni foam; — + C-coated & mixed with C on Ni foam.



**Fig. 8:** Cyclic polarisation curves of  $Mg_{63}Ni_{30}Y_7$  in 6 M KOH before and after hydrogen charging.

$C_{max} = 216$  mAh/g is obtained in the 5. cycle. The longer activation period is related to a stronger passivation ability of the amorphous powder [10]. These  $C_{max}$  obtained for  $Mg_{63}Ni_{30}Y_7$  electrodes are higher than those for other electrodes prepared and tested under similar conditions, e.g. mechanically alloyed  $Mg_2Ni$  (100–200 mAh/g) [3],  $Mg_{1.95}RE_{0.05}Ni$  (180–200 mAh/g) [11],  $Mg_{2-x}Al_xNi$  (105–175 mAh/g) [3] and comparable with  $Mg_{1.5}Mn_{0.5}Ni$  (241 mAh/g) [3]. Furthermore, the electrode performance strongly depends on the electrode design. Coating of the alloy powder particles with graphite powder by an additional short gentle milling and mixing these alloy powders with graphite powder result in significantly enhanced  $C_{max}$  values already in the first cycle (Fig. 7), i.e. 435 mAh/g for amorphous powder-based electrodes and 570 mAh/g for nanocrystalline powder-based electrodes. This strong improvement is attributed to a reactivity enhancement of alloy particle surfaces due to the active graphite coating and to an expansion of the metal-electrolyte interface due to a better penetration of the electrolyte into the less dense graphite-containing electrode composite. Both give rise to a higher electrode reactivity for the hydrogen reduction and in result, to a higher hydrogen sorption rate. However, for all electrodes longer cycling leads to degradation, mainly corrosion. After 10 cycles only 30–35 % of their  $C_{max}$  is retained. To describe these corrosion phenomena in more detail, electrochemical studies were performed on  $Mg_{63}Ni_{30}Y_7$  ribbons with defined surface area [12]. Fig. 8 shows cyclic polarization curves of samples in the as-quenched state and after severe cathodic hydrogen charging. The non-treated sample exhibits a spontaneous passivation behaviour due to  $Mg(OH)_2$  and  $Y(OH)_3$  formation. Only weak oxidation peaks related to a gradual nickel oxidation occur at low anodic potentials. During cathodic charging the ribbon sample absorbs hydrogen (>1.1 wt.%), meanwhile the surface chemistry changes remarkably. The cathodic loading further stabilizes  $Mg(OH)_2$  and  $Y(OH)_3$ , but also supports the gradual formation of “active nickel” and metastable nickel hydrides, which are oxidized during the following anodic polarisation. During repeated cycling this leads to a gradual materials degradation. Thus, for improving the cycle life performance further alloy modification and optimisation of the electrode design will be necessary.

## References

- [1] K. Hong, *J. Alloys Compd.* 321 (2001) 307
- [2] J. J. Reilly, *Z. Phys. Chemie NF* 117 (1979) 155
- [3] A. Gasiorowski et al., *J. Alloys Compd.* 364 (2004) 283
- [4] Y. Zhang et al., *Electrochim. Acta* 47 (2002) 1739
- [5] Z. M. Wang et al., *J. Alloys Compd.* 381 (2004) 234
- [6] A. Teresiak, A. Gebert, M. Savyak, M. Uhlemann, Ch. Mickel, N. Mattern, *J. Alloys Compd.* 398 (2005) 156
- [7] V. Rangelova, T. Spassov, *J. Alloys Compd.* 345 (2002) 148
- [8] A. Teresiak, M. Uhlemann, J. Thomas, A. Gebert, *Z.f. Kristallographie* 2006 (in press)
- [9] T. Spassov et al. *Mater. Sci. Eng.* A375–377 (2004) 794
- [10] B. Khorkounov, A. Gebert, Ch. Mickel, L. Schultz, *J. Alloys Compd.* 416 (2006) 110
- [11] Z. M. Wang et al., *J. Alloys Compd.* 381 (2004) 234
- [12] A. Gebert, B. Khorkounov, U. Wolff, Ch. Mickel, M. Uhlemann, L. Schultz, *J. Alloys Compd.* 419 (2006) 319

**Cooperations** Institute for Materials Science, Academy of Science of Ukraine, Kiev, TU Darmstadt

**Funded by** DFG (Projekt Ge 1106/3)

## Simulation of nanostructured surfaces for ARXPS

S. Oswald, F. Oswald, T. Gemming

Angle-resolved X-ray photoelectron spectroscopy (ARXPS) is a commonly used method for non-destructive depth profiling in the nanometer thickness range. To quantify the measuring data, model calculations are used which usually approximate the surface structures by smooth layers. This is often not realistic because surface and interface roughness can influence the results. We developed a computer algorithm for the simulation of ARXPS measuring results for virtually any near-surface materials distribution. Thus a various number of model structures for surface roughness could already be considered. The widely discussed "magic angle concept" for overlayers was critically examined. For various small sized inhomogeneous structures it could be concluded that in general an overestimation of the real surface coverage occurs as a result of edge and shadowing effects. Furthermore a systematic underestimation of the "amount of material" of the overlayers is found. It must be stated that the information content of ARXPS data is very limited for lateral structures in the nm range.

The current trend to micro-scaled material immediately leads to the demand of a highly sophisticated analysis of such nanometer-sized features. Besides an enormous development in transmission electron microscopy (TEM) also the classical surface spectroscopic analytical methods are still in the focus of interest. One promising method for non-destructive depth-profile analysis is the angle-resolved X-ray photoelectron spectroscopy (ARXPS). Depth information about the first some nm can be collected, because the effective information depth varies with changing the measuring angle. For quantitative interpretation, however, always model calculations are necessary. The ARXPS measurement results have to be compared with those from intensities calculated for an assumed model structure of the surface region. The parameters (thicknesses, stoichiometry, surface coverage) of the model structure are varied and the best approach of the calculated to the experimental results is searched for. This is a complicated process because the found results are very sensitive to the used model assumptions and boundary conditions, and generally their information content is very limited [1].

As a consequence, mostly simple models with smooth layers (at most with islands on top) are used up to now for the ARXPS quantification. However, it is quite clear that this is a wrong assumption in most of the real cases: all realistic surfaces have a roughness and may have lateral inhomogeneities. As demonstrated in Fig. 1 for a schematic rough surface it can be clearly assumed that the measuring results are influenced markedly. In our own recent work on the study of the growth of thin diffusion barriers [2-4], of oxide-oxide-interfaces [5, 6] and on nanoparticles as growth centers for nanotube structures [7] such effects also have been considered and discussed as limiting factors.

In order to quantify a possible misinterpretation, we decided to make computer simulations of ARXPS results for nanostructured surfaces. The newly developed simulation program [8] is based on a calculation of a large number of electron trajectories in an artificial surface volume that can be filled with any materials distribution. The attenuation of the signal electrons is described by an exponential law, using attenuation lengths calculated with the CS2 (Cumpson-Seah-2 [9]) formula; elastic scattering is neglected up to now. As an example material system we used  $\text{Al}_2\text{O}_3$  overlayers on top of Al substrates. Figure 2 demonstrates some used model surface structures: faceted surfaces with homogeneous oxide overlayer (a,b), oxide islands on Al substrate (c) [8], and islands and pores at an oxide layer (d,e) [10, 11]. The orientation of the  $x$ - $y$ - $z$ -scales, of the polar angle  $\theta$  (to the surface normal) and of the azimuth angle  $\phi$  is given there. The material parameters are stored in an array ( $x*y*z$ ) with a maximum size of  $1000*1000*1000$  with typical step width of  $1/100 \dots 1/50$  nm, thus inhomogeneous material regions of about  $10 \dots 20$  nm size can be modeled. Typically  $10^6$  electrons were

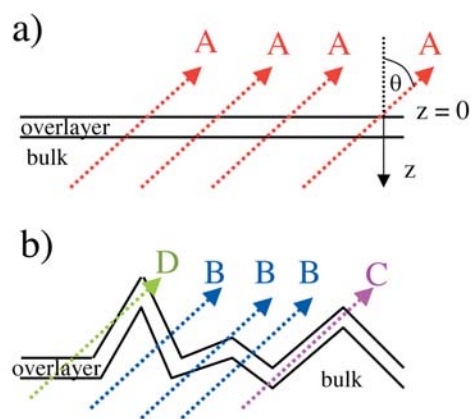


Fig. 1: Schematic view of similar electron paths at a rough surface (b) in comparison with an ideal flat surface (a). For the smooth surface, all measured electrons (A) have an identical path. With roughness several differences occur: (B) different emission angles, (C) long path in the overlayer, (D) shadowing.

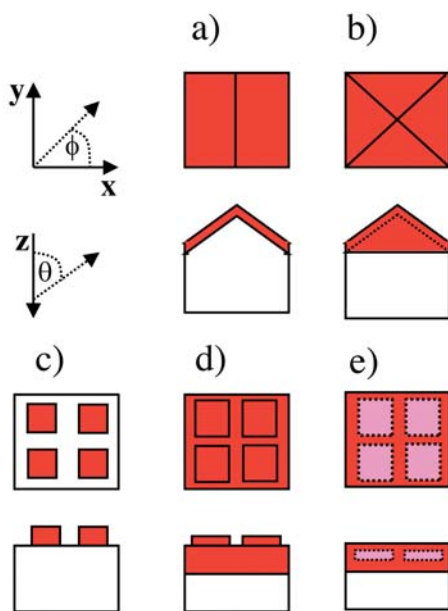
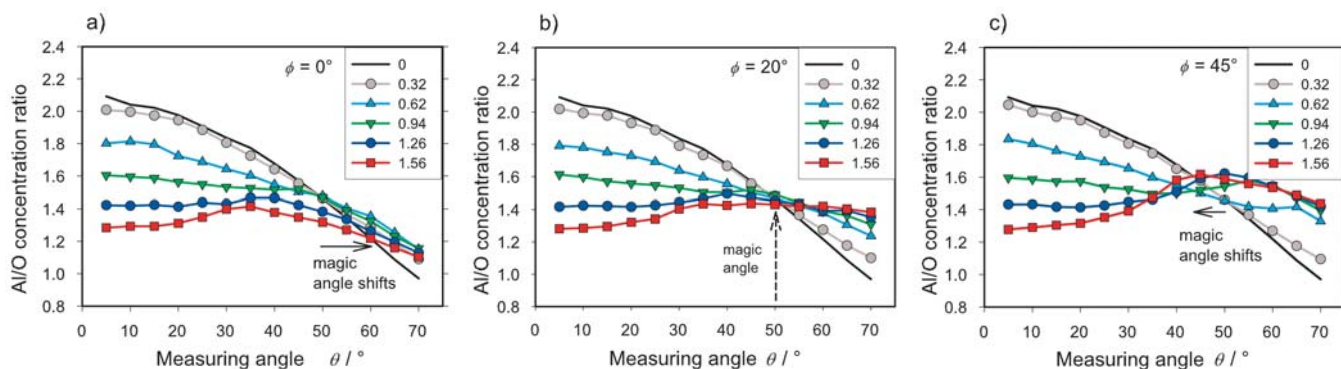


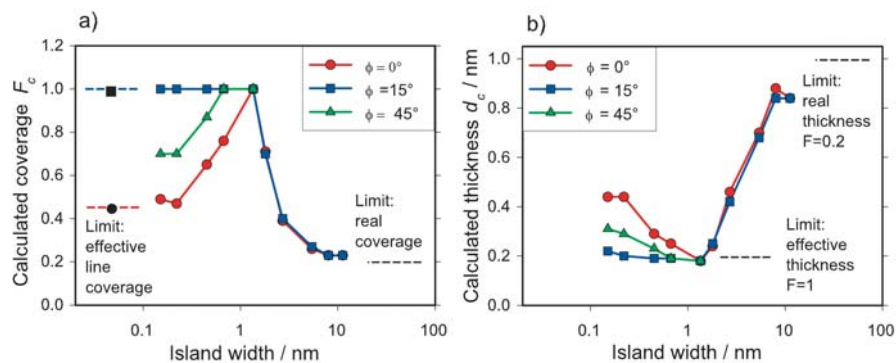
Fig. 2: Schemes of the Al/Al oxide (white/red) structures modeled in top and side view: facets (a), pyramids (b), islands - as an example with 4 islands per simulated structure (c), surface roughness as islands (d), or hollows/pores (e) in combination with a smooth overlayer. The Al substrate is white and the Al oxide structures are gray. The solid arrows give the coordinate system; the dotted arrows show the orientation of the simulated measuring angles.



**Fig. 3:** Results of ARXPS measurement simulations for an Al sample with pyramids on top covered with a 1 nm thick Al oxide overlayer (see the structure in Fig. 2b). The calculated concentration ratios Al/O are plotted as a function of the polar emission angle for different azimuth angles of  $0^\circ$  (a),  $20^\circ$  (b) and  $45^\circ$  (c) and various slopes (see insets) of the pyramids. A „magic angle“ of about  $50^\circ$  is found for all azimuth angles only for slopes below 1.

One topic of practical relevance is the search for measuring conditions, the so-called “magic angle”, at which a reliable determination of the overlayer thickness for rough samples is possible with the smooth layer approximation. We made calculations following the work of Gunter et al. [13] who found a magic polar angle of  $35 - 40^\circ$ . We considered overlayers on top of facets (stretched along the y-direction with triangular cross section = 2-dimensional roughness) and on pyramids (with a square base plane = 3-dimensional roughness) [8] as illustrated in Figs. 2a,b. In Fig. 3 results are shown for pyramids covered with a 1 nm Al oxide layer observed at 3 different azimuth angles ( $0^\circ$ ,  $20^\circ$ ,  $45^\circ$ ); parameter is the slope of the pyramid areas (roughness parameter). For low roughness (low slope) a magic angle (that is, the regions where the curves are crossing) of about  $50^\circ$  is found, for higher slopes this angle changes. This is in agreement with other studies where magic angles higher than previously assumed and dependent on the type of roughness were predicted.

**Fig. 4:** Results of ARXPS model calculations using the standard algorithm (unlimited island width) to approximate simulated measurement results for small Al oxide islands (thickness  $d = 1$  nm) of varying size with the surface coverage fraction  $F = 0.2$  on an Al substrate (see the structure in Fig. 2c). The parameter (see inset) is the azimuth angle. The calculated surface fraction  $F_c$  (a) and the calculated thickness  $d_c$  (b) are plotted against the island width. For small-sized islands, the fraction is overestimated, reaching values up to  $F_c = 1$  - the islands are described as smooth layers!



The study of thin film growth or surface segregation often is connected with island formation. We modeled island-like overlayers using islands with quadratic base plane and different size [8] according to Fig. 2c. Figure 4 shows results for Al oxide islands (surface fraction - ratio of covered to total surface area  $F = 0.2$ , thickness 1 nm, azimuth angles  $0$ ,  $15$ ,  $45^\circ$ ), which were reached with the standard smooth-layer ARXPS approximation. As expected, for the islands large in size the nominal surface fraction and island thickness is found. With lower lateral island size an increase of the calculated fraction up to a value of 1 is observed (Fig. 4a), that is, the island-covered surfaces then are

characterized as covered with a smooth oxide overlayer with lower thickness (Fig. 4b). Also for other surface fractions, different island thickness and model structures (buried islands) this general behavior was confirmed.

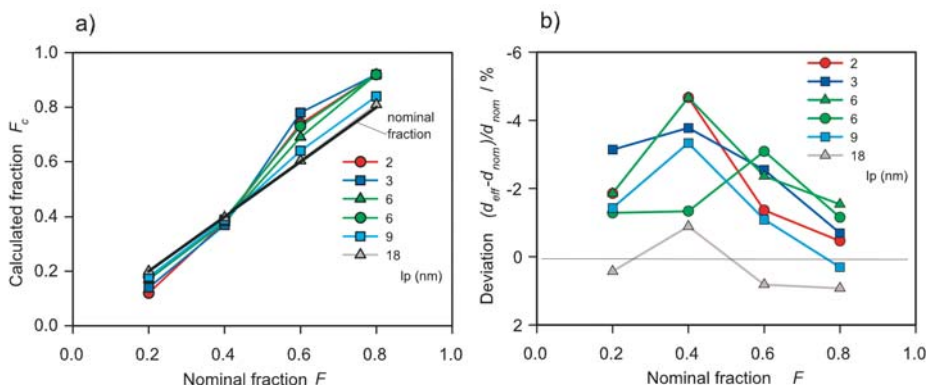


**Fig. 5:** Results for Al oxide islands of 1 nm height on a 0.5 nm thin Al oxide interlayer at an Al substrate for different surface fractions  $F$  and variation of the lateral size (periodicity  $lp$ ): (a) the calculated fraction  $F_c$  for the best fit, the relative deviation of effective thickness  $d_{eff}$  from the nominal thickness  $d_{nom}$  (b). Virtual homogenization leads to an increase of the high fractions and a decrease of the low fractions. The effective thickness shows a systematic underestimation depending on both the structure and the model used.

Closed layers with roughness were approximated as a combination of a smooth layer combined with islands, hollows and pores according to Fig. 2d,e. In Fig. 5 results are shown for 1 nm thick oxide islands on a 0.5 nm thick smooth oxide interlayer, varied in island surface fraction and lateral island size (parameter  $lp$  = distance between the islands). Similar to the island case (Fig. 4) for large islands the nominal fractions are reached, for small islands at least for the low and high coverage a tendency to homogenization is found - higher and lower fractions are found as best approximations. Quantitatively, however, the closed layer influences the results, i.e. the deviations from the nominal fraction are not as large as found before. In Fig. 5b the relative deviations of the amount of oxide material is given: the deviation of nominal thickness of the oxide material  $d_{eff}$  from the exact values  $d_{nom}$  is plotted. For the large islands the true values are calculated but for the smaller islands deviations up to 4% are found; in all cases the thickness is underestimated. The values for the largest fraction  $F = 0.8$  are the smallest; obviously because this situation is the nearest to a homogeneous layer. It must be noted here, that when using different starting conditions for the calculations, especially for the medium fractions (0.4 and 0.6) also different solutions with very good approximation can be found. Obviously a large number of local minima exists, which approximate the ARXPS intensities well. Nevertheless, all these solutions then are close to fraction 0 or 1 confirming the trend to a “homogenization”.

Many calculations at different nanometer-sized structures showed that with lowering their dimensions they can be described well as nearly homogeneous layers [11], with only a systematic under-representation of the effective amount of material. As an example in Fig. 6 results are presented for inhomogeneities with 1 nm thickness at a structure of 1.5 nm total height at several fractions and lateral structure sizes. The nominal thickness (6a) and the relative deviation of the calculated effective thickness from the nominal one (6b) are plotted. The following facts can be derived: as found before the nominal thickness is systematically underestimated, the lowest deviations (arrows) are found for the highest thicknesses - nearest to the closed layers, and the deviations increase slightly from the islands to the pores (green line).

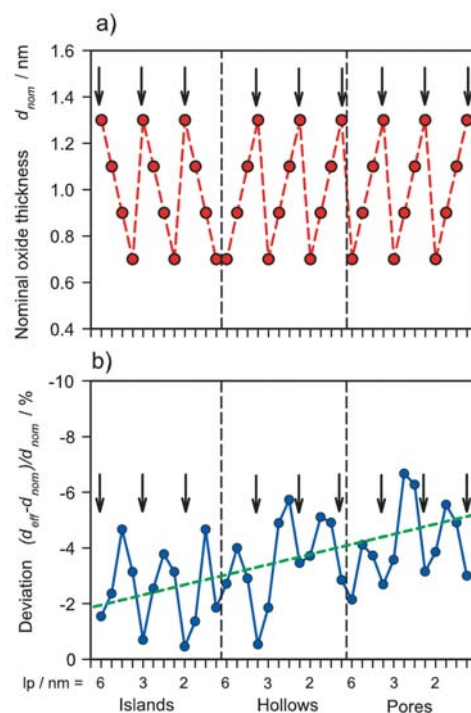


**Fig. 6:** Comparison of the nominal thickness (a) and the deviation of  $d_{eff}$  from  $d_{nom}$  for islands, hollows and pores of 1 nm thickness at a surface oxide layer of total 1.5 nm fractions  $F = 0.2, 0.4, 0.6, 0.8$  and different lateral width. Always an underestimation of  $d_{nom}$  is found, at the highest fractions (arrows) the lowest deviations are visible (see also Figs. 5b, c), and the deviation increases with more complex structure (green line).

The presented method for computer simulation of ARXPS measurements can be used effectively for the study of artifacts occurring at nanostructured surfaces. Using the standard quantification algorithms (smooth layers with islands on top) a general overestimation of the surface fraction, i.e. a trend to a homogenization was found due to edge and shadowing effects. If the spatial dimensions are in the range (or below) of the attenuation length of the electrons even smooth and homogeneous overlayers are good approximations for surfaces, which are rough in reality. Nevertheless, in such cases the amount of overlayer material is approximated, but always a systematic underestimation

is found. This is also an indirect result of the trend to homogenization: the material is artificially denser packed and leads with lower thickness to the same measured intensities. Thus it can be summarized that a quantitative characterization of surfaces with microroughness by means of ARXPS seems to be nearly impossible. In general the investigation of small sized features by ARXPS is much more problematic than widely assumed. In the future the systematic study of problems with local minima, the limited accuracy and elastic scattering will be the main topic of our theoretical work with the aim to give practical limits for the use of ARXPS in surface characterization.

#### References

- [1] P.J. Cumpson, *J. Electron Spectrosc. Rel. Phenom.* **73** (1995) 25
- [2] M. Zier, S. Oswald, R. Reiche, K. Wetzig, *Appl. Surf. Sci.* **252** (2005) 234.
- [3] M. Zier, S. Oswald, R. Reiche, M. Kozłowska, K. Wetzig, *J. Elect. Spect. Rel. Phenom.* **137-140** (2004) 229
- [4] M. Zier, S. Oswald, R. Reiche, K. Wetzig, *Microchimica Acta* **156** (2007) 99
- [5] R. Reiche, S. Oswald, F. Yubero, J.P. Espinos, J.P. Holgado, A.R. González-Elípe, *J. Phys. Chem. B* **108** (2004) 9905
- [6] C. Mansilla, M. Zier, R. Reiche, S. Oswald, J.P. Holgado, J.P. Espinós, F. Yubero, A.R. González-Elípe, *Surf. Interface Anal.* **38** (2006) 510
- [7] S. Oswald, R. Reiche, M. Zier, K. Wetzig, *Surf. Interface Anal.* **38** (2006) 590
- [8] S. Oswald, F. Oswald, *J. Appl. Phys.* **100** (2006) 104504
- [9] P.J. Cumpson, M.P. Seah, *Surf. Interface Anal.* **25** (1997) 430
- [10] S. Oswald, F. Oswald, *phys. stat. sol. (c)*, accepted
- [11] S. Oswald, *Surf. Sci.*, submitted
- [12] M. Kozłowska, R. Reiche, S. Oswald, H. Vinzelberg, R. Hübner, K. Wetzig, *Surf. Interface Anal.* **36** (2004) 1600
- [13] P.L.J. Gunter, O.L.J. Gijzeman, J.W. Niemantsverdriet, *Appl. Surf. Sci.* **115** (1997) 342

**Cooperation** AMD Saxony Dresden, FZ Rossendorf, TU Dresden, CSIC Sevilla

**Funded by** BMBF, SMWA, DFG



## Success in Technology Transfer

### From inventions to patents to innovations

W. Pfeiffer

In addition to research results achieved, it is the registration of inventions and patents granted that are an important gauge of the competency of any research institution. Also in 2006 IFW was able to continue its successful activities in this field. By 31 December 2006 the institute had been granted a total of 111 patents registered within Germany and 140 patents registered abroad. In the year 2006 a total of 9 inventions were registered and patent applications filed for them; 6 patents were granted to IFW within Germany and 4 abroad in 2006. For the purpose of a more efficient and professional handling of patent applications in terms of economic exploitability, renewal and decision on an international extension of applications, a so-called „property rights commission“ was established, and became already active, in 2006. In this body, which is chaired by the technology transfer officer, inventors, the patent lawyer, competent managers and representatives of WTR discuss the individual patent matters in great detail and strict consideration of economic and cost aspects, and advise the managing board on the decisions to be made.

The intensified efforts made to achieve a better exploitation of patents has resulted in three new licence agreements with industrial partners, with the agreement entered into with Vacuum Generators (UK) on the licensed manufacture of the IFW-developed cryomanipulator being rated as especially worth mentioning.

As regards further co-operation in the field of research and economic exploitability, the following 2006 patent applications can also be considered to be of great importance:

- A patent application filed jointly by IFW scientists and research technicians; the invention described is a method for the pyrometric measurement of the melted mass temperature in monocrystal growing systems. This is a promising practical improvement of crystal growing processes as a whole.
- Another patent application extends IFW's already comprehensive patent portfolio in the fields of alloying technologies and the manufacture of amorphous metals, and refers to moulded components subjected to high stresses as they are, for example, used in the aircraft industry, in competitive sport or machine construction. The invention describes a method for making high-strength mouldings of iron alloys which have plastic properties at room temperature and, in contrast to metallic glasses, are characterized by a macroscopic plasticity, deformation resistance and a significant strength increase.
- A further patent application refers to a manufacturing method for coated nano-tubes which has considerable advantages over conventional methods; fields of application for such coated nano-tubes are nano-structured catalysts in industrial chemical processes or their use as contact material in microelectronics and nanoelectronics.



Fig.1: Demonstrator SupraTrans at the „Ideenpark“ 2006 in Hanover

### Successful presentations

By way of selected performance presentations at international fairs, IFW made great efforts also in 2006 to establish new co-operation partnerships and canvass new projects. As an exhibitor at the Hanover industrial fair, IFW showed at the common SuperConductingCity stand (initiated by VDI) interesting exhibits from its range of newly developed strip-type superconductors and solid high-temperature superconductors that found the undivided attention of the visitors.



In connection with the new superconducting levitation vehicle models, the SupraTrans Demonstrator was undoubtedly a visitor magnet; they were shown in the „IDEENPARK ZUKUNFT“ exhibition area organized by ThyssenKrupp for the second time in Hanover in May 2006. This impressive promotion show was aimed at the future engineering staff and attracted more than 200,000 primarily young visitors.

The active support and participation of IFW Dresden in the events organized by the municipality of Dresden as the „City of Science 2006“ was an important aspect of the institute's public relations and technology transfer efforts; in these events, IFW showed most varied kinds of exhibits and made numerous other contributions. One of the highlights organized by IFW and the Otto-von-Guericke Society was the demonstration of the famous Magdeburg hemispheres experiment on the Elbe meadows on 12 August 2006 in Dresden.

**Fig. 2:** Historical large-scale experiment with Otto-von-Guericke and his famous Magdeburg hemispheres experiment on the Elbe river meadows